Surface-Micromachined Thermal Conductivity Gas Sensors For Hydrogen Detection

Author: Shuoxi Chen

Daily Supervisor: Ir. Huaiwen Wu

Supervisor: Dr. Ir. Reinoud Wolffenbuttel

October 2010

Delft University of Technology

SURFACE-MICROMACHINED THERMAL CONDUCTIVITY GAS SENSORS FOR HYDROGEN DETECTION

Thesis

submitted in partial fulfillment of the requirements for the degree of

Master of Science

in

Electrical Engineering,

in the Department of Microelectronics, EEMCS

by

Shuoxi Chen

Electronic Instrumentation Laboratory Group

Faculty of Electrical Engineering, Mathematics and Computer Science

Delft University of Technology

Delft University of Technology Department of Electrical Engineering

The undersigned hereby certify that they have read and recommend to the Faculty of Electrical Engineering, Mathematics and Computer Science for acceptance a thesis entitled "**Surface-Micromachined Thermal Conductivity Gas Sensors for Hydrogen Detection**" by **Shuoxi Chen** in partial fulfillment of the requirements for the degree of **Master of Science**.

Committee members:

Prof. dr. ir. Gerard C. M. Meijer
Dr. ir. Reinoud Wolffenbuttel
Dr. Ger de Graaf
Ir. Huaiwen Wu
Prof. dr. B. Dam

Dated: October, 2010

Contents

Chapter 1

Introduction

1.1 Motivation and Objectives

Gas sensors are the devices which detect the presence of target gas leak. In recent years, gas sensors are increasingly used in the rapid growing markets of safety application systems, especially for hydrogen detection in automotive combustion or fuel cell applications [1, 2]. In such systems, a leakage of hydrogen gas needs to be detected before the hydrogen builds up an easily ignited explosive mixture with the ambient air when the hydrogen concentration reaches the lower explosive limit (LEL) of 4% [3] in air. Consequently, fast response time, low cost and low power consumption gas sensors are in great demand for hydrogen detection in safety applications.

Such fast response time, low cost and low power consumption gas sensors have experienced a revival due to the progress in silicon-based micro-electro-mechanical (MEMS) technology during the last two decades [4]. Silicon-based MEMS technology not only has made the fabrication of low cost miniaturized gas sensors possible, but also has provided the high-performance gas sensors which combine electrical and thermal functionalities within a single piece of silicon. These miniature MEMS gas sensors are several orders of magnitude smaller than conventional gas sensors, while their power consumption, response time and production costs are dramatically reduced [5].

1.2 Thesis Organization

The previous paragraphs have introduced the motivation and applications of the work presented in this thesis. An overview of the contents of this thesis is given below.

Chapter 2 Gas Sensors Overview

This chapter will first introduce the advantages of using physical gas sensor instead of chemical gas sensor, and thermal conductivity sensor is a kind of physical gas sensor. Secondly, the basic principal of thermal conductivity gas sensors will be described. Finally, several advanced and representative gas sensors will be described and compared.

Chapter 3 Sensor Design Based on Analytical Approach

In this chapter, the thermal conductivity gas sensor design based on analytical approach will be presented. Firstly, the detailed principle of thermal conductivity based gas sensor will be explained. Secondly, the advantage of utilizing surface micromachining technology and the details in fabrication process will be clarified. Thirdly, the thermal modeling will be illustrated, and the formulas of sensor resistor temperature and sensor sensitivity will be derived. Finally, the optimal sensor sensitivity will be obtained based on analytical simulations using the derived formulas in Matlab software.

Chapter 4 Sensor Design Based on Numerical Analysis

In this chapter, the sensor design based on numerical analysis will be presented. Firstly, the sensor will be modelled based on the finite element method (FEM) simulation using COMSOL Multiphysics software. Two application modes - the conductive media DC and heat transfer modules are combined into a single model for interaction simulation using the multiphysics features of COMSOL Multiphysics. Then, the relationship between sensor sensitivity and different features of sensor will be derived based on numerical simulations in COMSOL. Finally, the optimal sensor sensitivity will be obtained based on the simulation results in COMSOL.

Chapter 5 Measurements and Validation

In this chapter, four measurement setups will be presented to show the validation of vacuum pressure measurement and carbon dioxide detection based on this thermal conductivity gas sensor. Vacuum pressure measurement was implemented to obtain the accurate results of the sensitivity of sensor devices with different features. For safety consideration, the carbon dioxide is utilized instead of hydrogen in the measurements. Besides, the thermal conductivity difference between carbon dioxide ($0.01465\,{}^{\mathrm{W}}/_{\mathrm{m\cdot k}}$) and air is only 5.93% of that between hydrogen and air; consequently, an achievement in carbon dioxide detection means an extremely high sensor sensitivity to hydrogen detection.

Chapter 6 Conclusions

This chapter concluded the thermal conductivity gas sensor on its application, principle, fabrication, analytical analysis, numerical analysis, measurements and sensor performance.

1.3 Summary: Original Contributions

The **main original contributions** in this thesis can be found in:

- The thermal modeling, formulas derivation and design optimization of the sensor sensitivity based on analytical analysis in Matlab are presented in Chapter 3.
- A optimal sensor with a **single-clamped** bridge structure and **larger gas openings**, and optimized based on numerical analysis in COMSOL Multiphysics has been achieved in Chapter 4. Compared with the original gas sensor model, the optimal sensor sensitivity is **5.17 times** higher.

Chapter 2

Gas Sensors Overview

This chapter will first introduce the advantages of using physical gas sensor instead of chemical gas sensor, and thermal conductivity sensor is a kind of physical gas sensor. Secondly, the basic principal of thermal conductivity gas sensors will be described. Finally, several advanced and representative gas sensors will be described and compared.

2.1 Gas Sensors Classification

There are two fundamentally different approaches for gas sensor: chemical sensor and physics sensor. Chemical gas sensing is based on the measurement of a change in electrical conductance or other physical properties of the sensing material due to the chemical interaction between the gas and the sensing material. There is a major problem in chemical gas sensors: the long-term stability is limited due to the contamination of the interface during chemical interaction [5, 6, 7].

Another major drawback of chemical sensors is the slow response time due to their chemical interaction is strongly dependent on environment temperature. For instance, palladium (Pd)-based chemical sensors are commonly used for hydrogen detection since Pd has a high sensitivity and selectivity towards hydrogen [3, 8, 9, 10, 11]. However, the Pd-based gas sensors often have a very slow response time at low temperatures due to their strong temperature dependence, from several hundred seconds to several minutes [3, 12, 13, 14] when detect 1% change in

the hydrogen concentration in air.

Therefore, the physical gas sensor that relies on the direct measurement of a physical property of a measured gas is better, since it offers possibilities for an enhanced long-term stability and a fast response time. Especially, the thermal conductivity sensor is such a good solution. Although **thermal conductivity sensors** are generally not as selective or sensitive as chemical gas sensors [5], they are **faster and more reliable since they will not be temperature depended or contaminated** when they sense the gases.

2.2 Thermal Conductivity Gas Sensors

Thermal conductivity sensors are especially suitable for the hydrogen detection, since the thermal conductivity of hydrogen ($0.1805\,{}^{\mathrm{W}}/_{\mathrm{m\cdot k}}$ [15]) is approximately 7.5 times that of the air ($0.02394\,{}^{\mathrm{W}}/_{\mathrm{m\cdot k}}$ [16]). It indicates that even very low concentration of hydrogen leakage in air is able to be detected due to the notable increase in gas thermal conductivity. Therefore, thermal conductivity gas sensors are especially suitable for the hydrogen leakage detection before hydrogen concentrations reach the lower explosive limit (LEL) of 4% in air in safety applications.

The basic principle of thermal conductivity based gas sensor will be presented in this section. Before that, the relevant background knowledge on heat transfer and thermopile will be introduced as follows.

2.2.1 Prerequisites

Heat transfer

Heat transfer is the transition of thermal energy from a material at a higher temperature to a material at a lower temperature [17, 18, 19]. There are three ways of heat transfer: heat conduction, convention and radiation.

Heat Conduction and Thermal Conductivity

Heat conduction is one of the most important ways of heat transfer in micro-scaled structure. By definition, heat conduction is the heat energy flows from the region of

high temperature to the region of low temperature, when there exists a temperature gradient within a body [18]. For example, a metal spoon placed in hot water can quickly conduct the heat through the spoon to your hand.

Heat conduction H can be defined as [20]:

$$H = \frac{\Delta Q}{\Delta t} = \lambda A \frac{\Delta T}{x} \text{ [W]} \tag{2.1}$$

where $\frac{\Delta Q}{\Delta t}$ is the rate of heat flow, λ is the thermal conductivity, A is the total cross sectional area of conducting surface, ΔT is the temperature difference, and x is the thickness of conducting surface separating the two temperatures.

Thermal conductivity is the property of a material that indicates its ability to conduct heat [20]. Thermal conductivity is measured in watts per Kelvin per meter ($\left[\frac{W}{m \cdot K}\right]$). Rearranging the equation 3.16 gives thermal conductivity [20]

$$\lambda = \frac{\Delta Q}{\Delta t} \cdot \frac{1}{A} \cdot \frac{x}{\Delta T} \left[\frac{\mathrm{W}}{\mathrm{m} \cdot \mathrm{K}}\right] \tag{2.2}$$

which means that thermal conductivity can be thought of as a flux of heat $\frac{\Delta Q}{A \Delta t}$ divided by a temperature gradient $\frac{\Delta T}{x}$.

Thermal conductance is the quantity of heat that passes in unit time through a plate of particular area and thickness when its opposite faces differ in temperature by one kelvin, which is given by:

$$G = \frac{\lambda A}{x} \left[\frac{\mathrm{W}}{\mathrm{K}}\right] \tag{2.3}$$

where λ is the thermal conductivity, A is the area, x is the thickness of the plate.

Thermopile, Thermocouples and Seebeck Effect

A thermopile is an electronic device that converts thermal energy into electrical energy. It is composed of thermocouples connected in series.

A thermocouple is a junction between two different metals that produces a vol-

tage related to a temperature difference. Thermopiles do not measure the absolute temperature, but generate an output voltage proportional to a local temperature difference or temperature gradient.

The Seebeck effect is the conversion of temperature differences directly into electricity [21]. The effect is that a voltage is created in the presence of a temperature difference between two different metals or semiconductors.

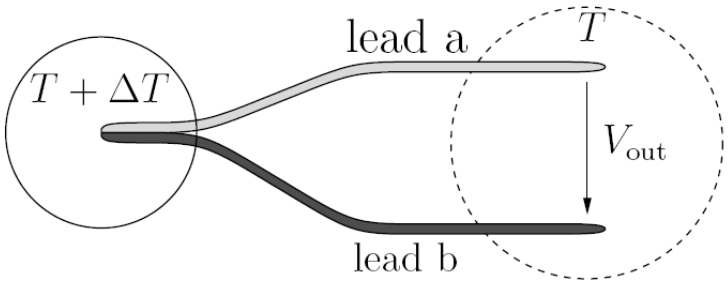

Figure 2.1: Thermocouple generate the thermoelectric voltage under temperature difference [22]

Figure 2.1 presents a thermocouple which consists of two different leads a and b. An open circuit voltage V_{out} is generated when the thermal potential on the junction is higher than that of the open end. The proportionality between the output voltage and the applied temperature difference ΔT is defined as Seebeck coefficient α_T. Seebeck coefficient is a temperature dependent material constant denoting the thermoelectric voltage generated by the thermocouple for an applied temperature difference [22]:

$$V_{out} = \alpha_T \cdot \Delta T \text{ [V]}$$

2.2.2 Basic Principle of Thermal Conductivity Gas Sensors

As shown in Figure 2.2, thermal conductivity gas sensors perform a measurement of the thermal conductivity of measurand gas as follows.

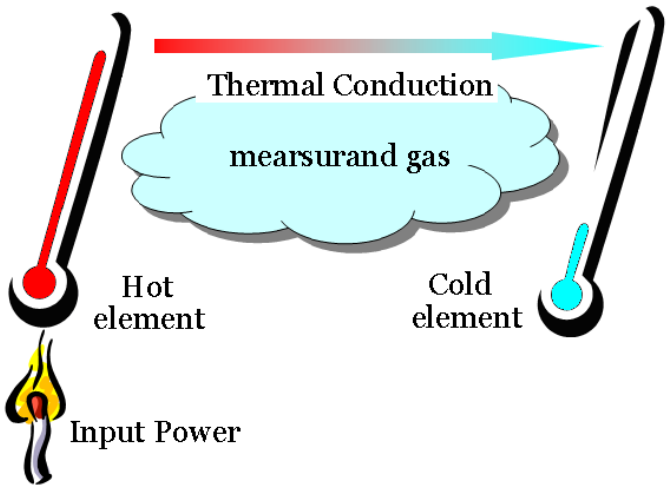

Figure 2.2: Principle of thermal conductivity gas sensor

The "hot element" is heated up by the supplied input power. Normally, the "hot element" is a resistor and heated up by feeding input current or voltage. Then, the measurand gas transfers a quantity of heat via thermal conduction from the "hot element" to the "cold element", which leads to a decrease in the temperature of "hot element". Because the quantity of heat conducted by measurand gas from the "hot element" depends on the thermal conductivity of measurand gas, as described in equation 2.1. Thus, for a given experimental configuration and a fixed input power, the changes in temperature of "hot element" depends on the thermal conductivity of measurand gas, so that **the changes in the thermal conductivity of measurand gas can be detected by measuring the changes in the temperature of the "hot element".**

2.2.3 Temperature Measurement

The changes in temperature of the "hot element" need to be detected simply, sensitively, reliably and inexpensively. One widespread method of temperature measurement is thermistor-based temperature measurement, typically platinum (Pt) resistors-based. The reason is that Pt resistors are superior in terms of accurate temperature coefficient of resistivity (TCR) and, therefore, have a better defined temperature dependence.

However, during the temperature measurement, one significant problem in Pt resistors-based temperature measurement is that the self-heating effect causes a temperature rise in the sensor element [23]. Self-heating effect is that when a current flows through a thermistor, it will generate heat which will raise the temperature of the thermistor above that of its environment [24]. If the thermistor is being used to measure the temperature of the environment, this electrical heating will introduce a significant error if a correction is not made. Besides this self-heating effect, Pt resistors are poorly IC-process compatible.

One of the temperature measurement methods which do not have the problem of self-heating or poorly IC-process compatible is thermopile-based temperature measurement. In additional, thermopiles have various attractive properties [23]:

1. Firstly, the thermopile is based on the self-generating Seebeck effect, this ensures that:

- The output signal generated by the thermopile which has no offset or no offset drift, because there cannot be any output signal without input power,
- the thermopile does not suffer from interference from power supplies or any physical or chemical signals except light (which can easily be shielded), because the Seebeck effect and the photoelectric effect are the only two self-generating effects in silicon,
- the thermopile does not need any biasing,
- the read-out circuit is quite simple, only a voltmeter is required.

2. Moreover, the sensitivity of the thermopile is hardly influenced by variations in the electrical parameters across the wafer or by the temperature. Unlike transistors and resistors, whose sensitivity and offset depend on the position on the wafer and the temperature.

Thus the changes in temperature of the "hot element" can be well detected by thermopile for its well IC-process compatible and none self-heating effect.

2.2.4 Sensor Sensitivity

As discussed before, the recommended method to measure the temperature changes of the "hot element" in thermal conductivity gas sensors is based on thermopile. Consequently, the output sensor signal is the Seebeck voltage generated by the thermopile. Thus at a given input power, the sensor sensitivity is defined as the ratio of the change in output Seebeck voltage $\Delta U_{seebeck}$ to the change in the measurand gas concentration in air. Assume the change in the measurand gas concentration in air is α, then the sensor sensitivity is expressed by:

$$S = \frac{\Delta U_{seebeck}}{\alpha} \text{ [mV]}$$

2.3 State of the art Gas Sensors

2.3.1 Gas-sensitive Metal based Chemical Gas Sensors

The gas-sensitive metal or metal oxide based chemical sensors are the most widely used commercial gas sensors in safety application systems, since they are high sensitivity and low cost [4, 25, 26, 27]. However, they normally suffer from the high power consumption due to their chemical interaction is strongly dependent on constant high environment temperatures.

An improved high-performance gas-sensitive metal based chemical sensor for hydrogen detection is described as follows.

Description

A micro gas-sensitive metal oxide chemical gas sensor [28] which was fabricated with surface micromachining process is shown in Figure 2.3. This gas sensor was mounted on a highly thermal isolated layer to reduce the heat loss to the substrate.

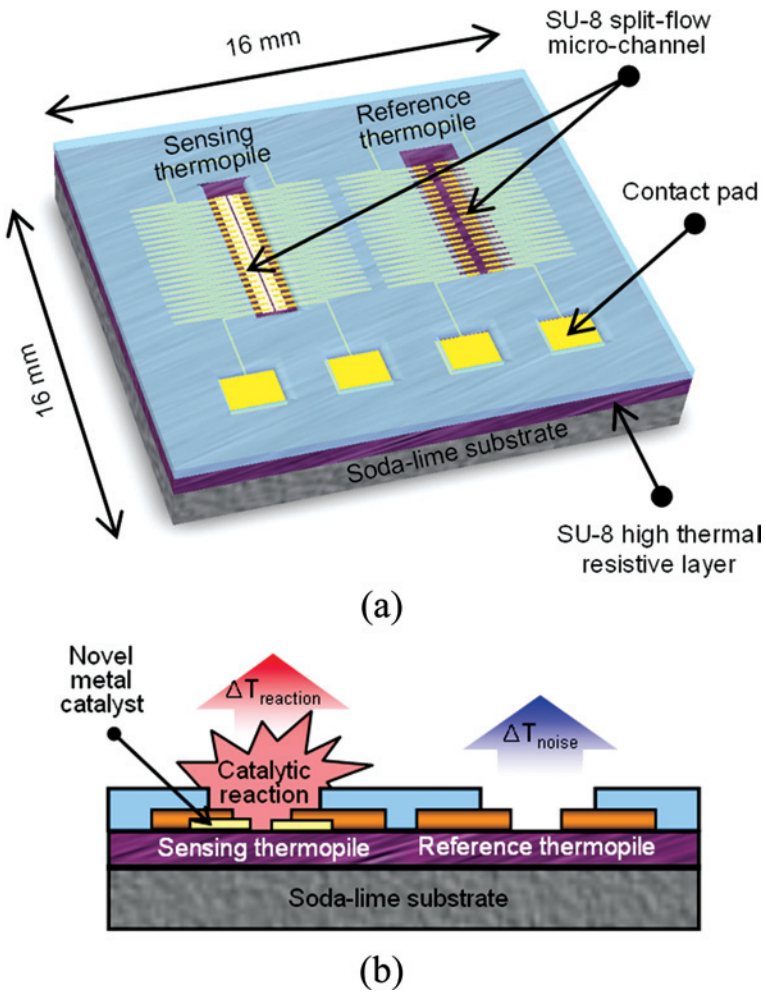

Figure 2.3: Schematic and sensing principle of micro-thermoelectric gas sensor (a) conceptual view (b) principle of the self-compensation method using the reference thermopile for reducing external thermal noise

The sensor structure consists of a gas-sensitive palladium catalyst and 60 Cu-Bi thermocouples. The catalytic reaction occurs only on the hot junction of the sensing thermopile where the palladium catalyst is deposited.

The gas sensor detects the target hydrogen by measuring the reaction heat of the catalytic reaction between the hydrogen and the palladium. The reaction heat is measured by thermopile. In order to reduce the external thermal noise, a difference between the output voltage of the sensing and the reference thermopiles was measured by a differential amplifier. The sensor output Seebeck voltage which generated

by thermopile linearly increased with the hydrogen gas concentration.

Advantages and Disadvantages

It is worth noting that this gas sensor does not need any heater, because it measures the reaction heat of the catalytic reaction between the hydrogen and the palladium. Secondly, palladium catalyst interaction requires less demand for environment temperature than conventional palladium-based chemical interaction, which leads to lower power consumption compared with conventional palladium-based chemical gas sensor. Thirdly, the external thermal noise is reduced by using a differential amplifier to measure a difference between the output voltage of the sensing and the reference thermopiles.

However, the required temperature for palladium catalyst interaction need to be constant which leads to a slow response time. In addition, the long-term stability of the sensor is limited due to the chemical contamination during the catalytic reaction.

2.3.2 Thermal Conductivity Gas Sensors

Compared with chemical gas sensors, thermal conductivity sensors offer possibilities for an enhanced long-term stability and a fast response time. Although thermal conductivity sensors are generally not as selective or sensitive as chemical gas sensors, they are faster and more reliable since they will not be contaminated when they sense the gases.

Two representative thermal conductivity gas sensors for hydrogen detection are shown as follows.

2.3.2.1 Thermal Conductivity Sensor TCG-3880

Description

The TCG-3880 is a commercial thermal conductivity gauge (TCG) which produced by Xensor Integration, the Netherlands [29]. In 2005, A.W. van Herwaarden described its detailed structure in [30].

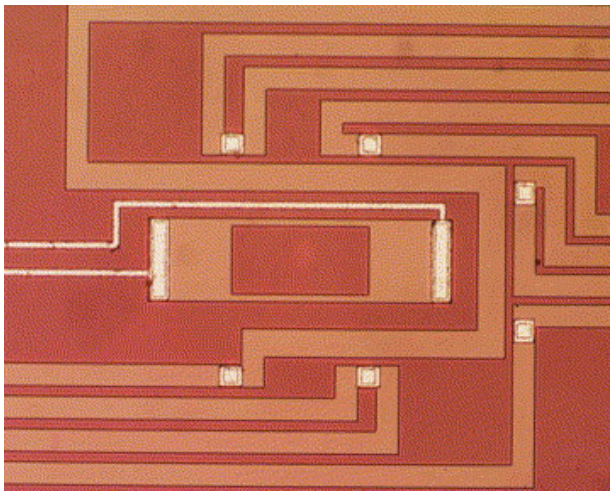

Figure 2.4: Central heater and hot junctions of thermopiles in TCG-3880

Fig 2.4 shows the central heater and the hot junctions of the p-type poly-Si and n-type poly-Si thermopile around it. By feeding current into the resistor in the center of the sensor, the resistor is heated up and becomes a "hot element". For a fixed input power, the resulting temperature of hot resistor (heater) mainly depends on the thermal conductivity of measurand gas. The thermopile measures the change in temperature of the hot resistor with the measurand gas concentration, consequently, detects the gas.

Advantages and Disadvantages

Advantages: this thermal conductivity sensor is long-term stable, low cost and has a very fast response time.

Disadvantages: its sensor sensitivity is relatively low compared with that of chemical gas sensor.

2.3.2.2 Micromachined Thermal Conductivity Sensor for Natural Gas Analysis

Description

In 2008 S. Udina etc. fabricated a micromachined thermal conductivity sensor for

natural gas analysis [31] as shown in Figure2.5.

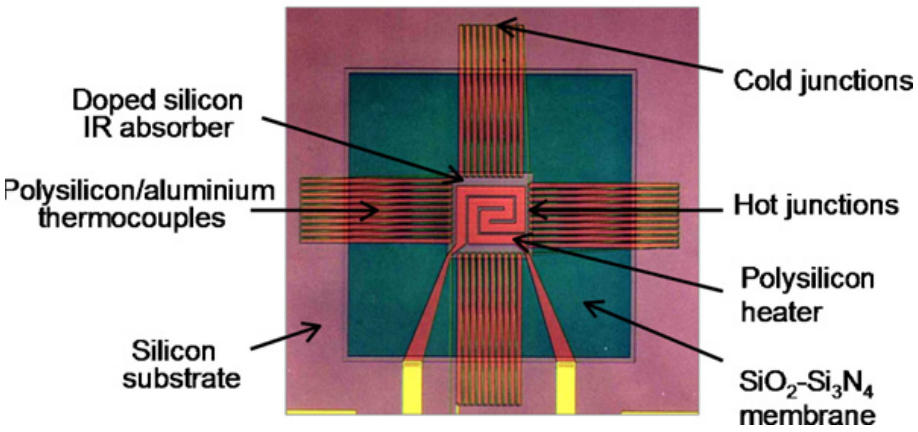

Figure 2.5: Fabricated micromachined thermoelectric sensor

By applying voltages to the polysilicon integrated resistive heater in the center of membrane, the resistive heater act like a "hot element" and the cold surrounding silicon rims are the "cold elements". The temperature difference is measured by 40 aluminum and n-doped polysilicon thermocouples. Therefore, for a fixed input power, the resulting temperature of the hot resistor (heater) mainly depends on the thermal conductivity of measurand gas. The thermopile measures the change in temperature of the hot resistor with the measurand gas concentration, consequently, detects the gas.

A thermal spreader, as shown in Figure2.6, is adopted here for a better temperature homogeneity across the hotplate . Consequently, an additional anisotropic wet etching process is needed for the spreader to eliminate the silicon from the backside.

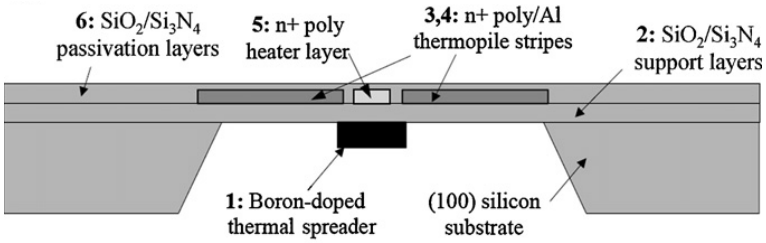

Figure 2.6: Cross-section of micromachined thermoelectric sensor

Advantages and Disadvantages

Advantages: this thermal conductivity sensor has a long-term stability, a high sensitivity and a very fast response time.

Disadvantages: the fabricated bulk-micromachining process is quite complicated which lower the yield of the device. And **the large amount of thermocouples will result in a relatively high thermal noise.**

2.4 Performance Evaluation

Sensitivity, response time, power consumption, stability, detection limit are the main performances that need to be considered in gas sensors [4]. The evaluation and comparison of the performances of state-of-art gas sensors mentioned in last section is shown in Table 2.1.

Table 2.1: Comparison of Sensors Performance

	Sensitivity [mV]	**Input Power** [mW]	**Sensitivity /Power** [V/W]	**Response Time** [s]	**Detection limit**	**Stability**
[28]	160 (Hydrogen in air)	Catalytic activation energy	–	7 s	0.1% - 2% Hydrogen	poor
[29]	48 (Hydrogen in air)	10.42	4.61 (Hydrogen in air)	36 ms	0.1% - 2% Hydrogen	good
[31]	250 (Ethane in methane)	59.50	4.20 (Ethane in methane)	–	–	good

Sensor sensitivity

For a given input power, thermal conductivity sensor [31] possesses a higher sensor sensitivity than TCG-3880 [29] since the thermal conductivity difference between hydrogen and air is 9 times higher than that between ethane and methane.

The large amount of thermocouples and the high thermal isolation of the membrane in thermal conductivity sensor [31] **are of great importance to en-**

hance its sensor sensitivity. However, the large amount of thermocouples will result in a high thermal noise.

Response time

Thermal conductivity sensor TCG-3880 [29] has a much faster response time than Pd catalyst chemical sensor [28]. Although the Pd catalyst chemical sensor [28] is much faster compared with conventional chemical sensors, its response time is still slower compared with thermal conductivity sensors due to its catalyst chemical interaction is strongly dependent on the environment temperature.

2.5 Conclusion

- **Thermal conductivity sensors are especially suitable for hydrogen detection, since the thermal conductivity of hydrogen is approximately 7.5 times that of the air.** It indicates that even **very low concentration of hydrogen leakage** in air is still possible to be detected. Therefore, thermal conductivity gas sensors are especially suitable for the hydrogen detection before the hydrogen concentration reach the lower explosive limit (LEL) of 4% in air in safety applications.

- Thermal conductivity gas sensor performs a measurement of the thermal conductivity of measurand gas. The "hot element" is heated up by the supplied input power. The measurand gas transfers a quantity of heat via the thermal conduction from the "hot element" to the "cold element", which leads to a decrease in the temperature of "hot element". Thus, **the changes in the thermal conductivity of measurand gas can be detected by measuring the changes in the temperature of the "hot element" using thermopile.**

- Sensitivity, response time, power consumption, stability, detection limit are the main performances that need to be considered in gas sensors. **Thermal conductivity sensors have an enhanced long-term stability and a faster response time compared with chemical sensors. The large amount of thermocouples and the high thermal isolation of the membrane**

are of great importance to enhance the sensor sensitivity in thermal conductivity sensors. However, the large amount of thermocouples will result in a high thermal noise.

Chapter 3

Sensor Design Based on Analytical Approach

In this chapter, the thermal conductivity gas sensor design based on analytical approach will be presented. Firstly, the detailed principle of thermal conductivity based gas sensor will be explained. Secondly, the advantage of utilizing surface micromachining technology and the details in fabrication process will be clarified. Thirdly, the thermal modeling will be illustrated, and the formulas of sensor resistor temperature and sensor sensitivity will be derived. Finally, the optimal sensor sensitivity will be obtained based on the analytical simulations using the derived formulas in Matlab software.

3.1 Thermal Conductivity Sensors Detailed Principle

Thermal conductivity gas sensor performs a measurement of the thermal conductivity of measurand gas as follows. By feeding current into the resistor in the center of the sensor (the small red box in the middle of Figure 3.1), the resistor is heated up and becomes a "hot element". Then, the measurand gas transfers a quantity of heat from the hot resistor to the cold edge via thermal conduction through the measured gas and the suspended membrane, which leads to a decrease in the temperature of hot resistor. To achieve a high sensitivity, the sensor structure should be designed

to reduce the heat loss through the suspended membrane to negligible values, to ensure that the quantity of heat loss from the hot resistor is mainly determined by the thermal conductivity of measurand gas.

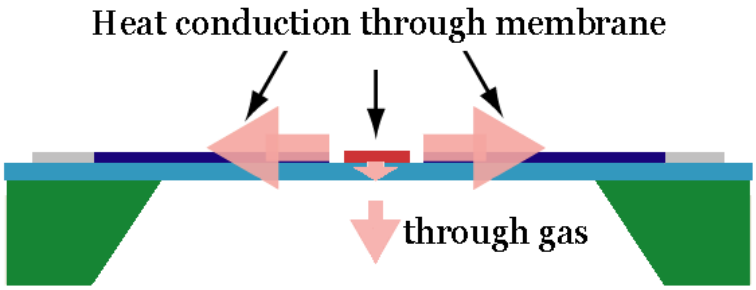

Figure 3.1: Principle of thermal conductivity gas sensor

Thus, for a given experimental configuration and a fixed input power, the changes in the temperature of hot resistor depends on the thermal conductivity of measurand gas, so that **the changes in the thermal conductivity of measurand gas can be detected by measuring the changes in the temperature of resistor**.

3.2 Fabrication Process

3.2.1 Surface-micromachining Process

To achieve a high sensitivity for micro-scaled thermal conductivity gas sensors, it is important to reduce the heat loss through the suspended membrane to negligible values. In previous studies, floating membrane structure of thermoelectric sensing layers which fabricated in bulk micromachining process was mostly used to minimize the heat loss to the suspended membrane. However, that method has a major drawback that lowering the yield of devices due to the complicated fabrication process by bulk micromachining.

Compared to bulk micromachining, surface micromachining is able to create much more complicated devices, capable of sophisticated functionality, which is suitable for applications requiring more sophisticated and cheaper mechanical elements [32].

Consequently, in order to improve the sensor sensitivity by minimizing the heat loss to the suspended membrane without any complex fabrication steps, a simple floating membrane structured micro-thermoelectric gas sensor is fabricated using surface micromachining as shown in Figure 3.2.

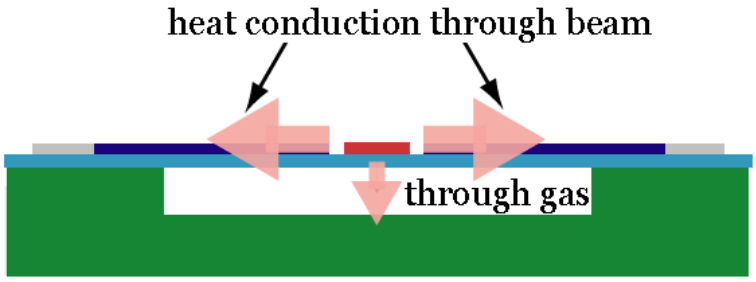

Figure 3.2: Principle of thermal conductivity gas sensor

3.2.2 Sensor Elements Design

The materials and structure of the heater and thermopile greatly determine the performance of the thermal conductivity gas sensor.

Heater

Although platinum (Pt) resistors are superior in terms of accurate temperature coefficient of resistivity (TCR) and, therefore, have a better defined heat generation, Pt resistors are poorly IC-process compatible. Therefore, P-type poly-silicon is utilized here for its acceptable linearity with temperature variation and relatively low thermal conductivity [33]. The meandered shape of the resistor enables high electrical resistance while occupying small area.

Thermopiles

The materials of the thermocouples strongly determine the sensitivity of the sensor. The P-type poly-silicon (Seebeck coefficient -120 μV/K) and N-type poly-silicon (Seebeck coefficient 170 μV/K) thermocouples are used here for their relatively high

Seebeck coefficients. They are connected in a thermopile configuration with ten pairs of thermocouples to increase the total Seebeck voltage.

3.2.3 Fabrication Processing Steps

The detailed fabrication process sequence is clarified in Figure 3.3.

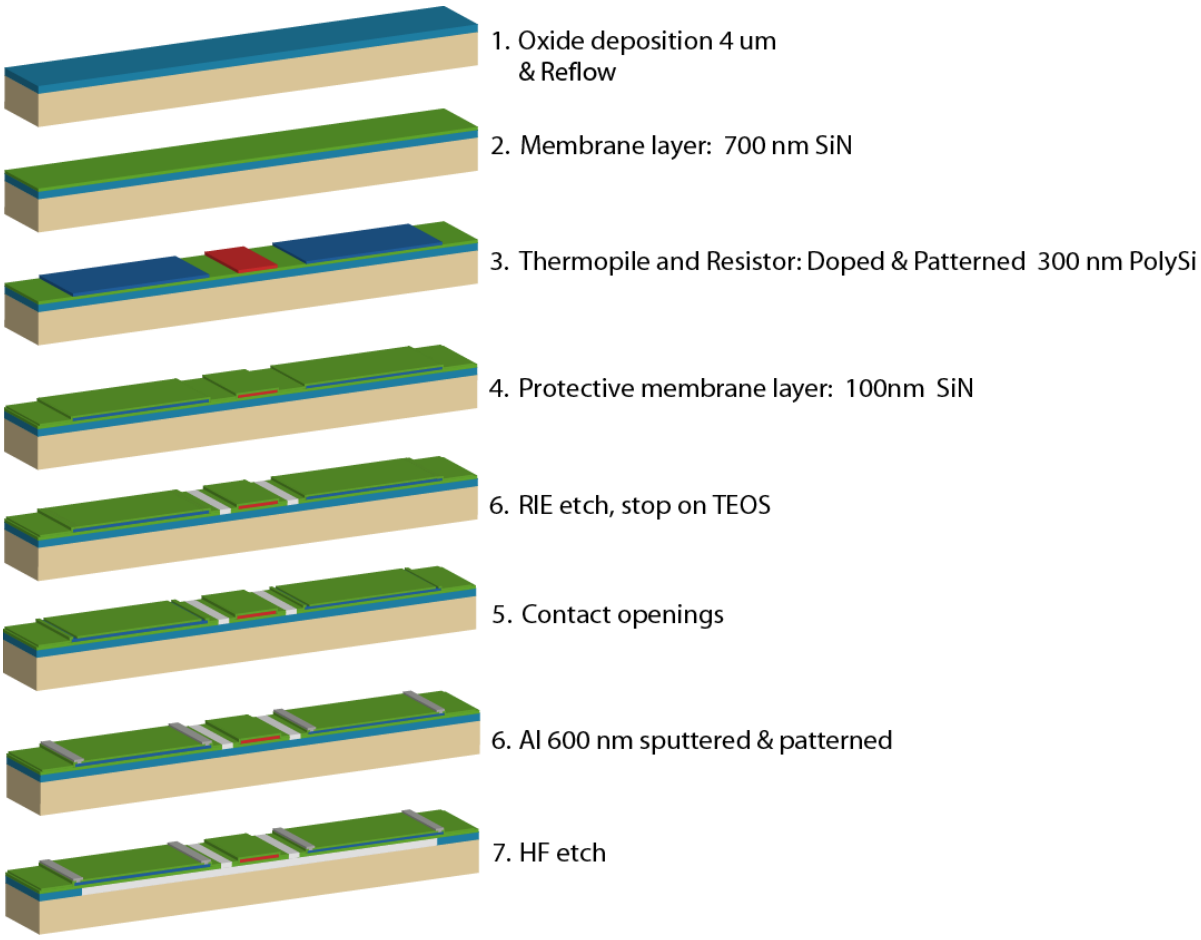

Figure 3.3: Fabrication processing steps

Fabrication of the TCD sensor was done in DIMES facility of the TU-Delft. The process sequence is shown in Figure 3.3. For complete processing of the device only six masks were needed. The fabrication starts with the deposition and reflow of the sacrificial layer of 4μm TEOS. On top of the oxide layer, a 700 nm layer of low

stress SiN film is deposited. Next, a 300 nm low-stress PolySi layer is grown by LPCVD. After this, boron is implanted at 40 keV to realize p-type PolySi. After a cleaning procedure, n-type PolySi is formed by phosphorous doping. In the next step, 100 nm SiN is deposited by LPCVD and patterned. A RIE etch, stopping on the sacrificial layer, is applied for defining the MEMS structures. Contacts to the PolySi are patterned and etched in the top SiN layer. Then aluminium is deposited and patterned on top to define the connections between the PolySi layers and the bonding pads. Finally, the wafer was processed with 73% high concentration HF since this does not attack the unprotected aluminium for 10 minutes for the surface-micromachining.

3.3 Thermal Modeling

The proposed gas sensor as shown in Figure 3.4 can be analyzed using a three-dimensional temperature distribution analysis, while the effect of thickness of the layers in this sensor can be disregarded due to all the layers are very thin films. The heat is transferred in two directions, one is in z-direction through the measured gas, and the other is in y-direction through the beam.

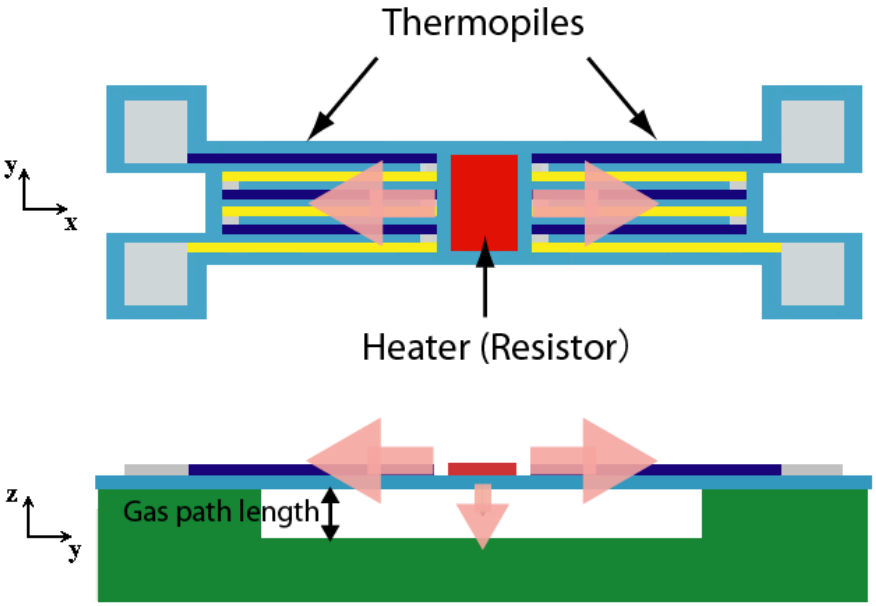

Figure 3.4: Three-dimensional temperature distribution of the gas sensor

3.3.1 Prerequisites

The basic knowledge, the heat equation and the law of heat conduction which will be used in the thermal modeling are introduced.

Convection

Convection is the heat transfer by mass motion of a fluid (such as air or water) when the heated fluid is caused to move away from the source of heat, carrying energy with it. There are two major types of heat convection:

1. Natural convection: when the fluid motion is caused by buoyancy forces that result from the density variations due to variations of temperature in the fluid.

2. Forced convection: when the fluid is forced to flow over the surface by external source, creating an artificially induced convection current.

Unlike at large scales, it is found that for a microscale heater, the natural convection from the heater to surrounding air is negligible and the heat loss is dominated by heat conduction [34].

Radiation

Thermal radiation is electromagnetic radiation emitted from a material due to the heat of the material. As stated in the Stefan–Boltzmann law, the total energy radiated per unit surface area of a black body ($\varepsilon = 1$) in unit time is directly proportional to the fourth power of the black body's absolute temperature T. Therefore, the total radiant power from the general grey body can be written as

$$P = \varepsilon \cdot \sigma \cdot A \cdot T^4 \text{ [W]} \tag{3.1}$$

where the constant ε is the emissivity factor, σ is the Stefan–Boltzmann constant which equals to $5.67 \times 10^{-8}[\frac{\mathrm{W}}{\mathrm{m^2K^4}}]$, and A is the radiating surface area.

Heat Equation

The heat equation is an important partial differential equation which describes the distribution of heat (or variation in temperature) in a given region over time. For

a function (x, y, z, t) of three spatial variables (x, y, z) and the time variable t, the heat equation is [35]

$$\frac{\partial T}{\partial t} = \alpha \left(\frac{\partial^2 T}{\partial x^2} + \frac{\partial^2 T}{\partial y^2} + \frac{\partial^2 T}{\partial z^2} \right) + \frac{\Phi_s}{\rho c_p} \tag{3.2}$$

where $\Phi_s$is the heat source power per volume V, and λ the thermal conductivity, and thermal diffusivity α which can be expressed as:

$$\alpha = \frac{\lambda}{\rho c_p} \left[\frac{\mathrm{m}^2}{\mathrm{s}} \right] \tag{3.3}$$

in which ρ is the density, and c_p is the constant pressure specific heat.

When the temperature is unchanging in time, which means the system in a steady state, then the heat equation is expressed as:

$$\frac{\partial T}{\partial t} = 0 \;\Rightarrow\; \alpha \left(\frac{\partial^2 T}{\partial x^2} + \frac{\partial^2 T}{\partial y^2} + \frac{\partial^2 T}{\partial z^2} \right) + \frac{\Phi_s}{\rho c_p} = 0 \tag{3.4}$$

with $\lambda \neq 0$, the heat equation is simplified as

$$\left(\frac{\partial^2 T}{\partial x^2} + \frac{\partial^2 T}{\partial y^2} + \frac{\partial^2 T}{\partial z^2} \right) + \frac{\Phi_s}{\lambda} = 0 \tag{3.5}$$

The Law of Heat Conduction

The law of heat conduction, also known as Fourier's law, states that the heat flux ϕ_q is equal to the product of thermal conductivity λ and the negative temperature gradient $-\nabla T$, as expressed by

$$\phi_q = -\lambda \nabla T \tag{3.6}$$

This equation determines the heat flux ϕ_q for a given temperature profile T and thermal conductivity λ. The minus sign ensures that heat flows down the temperature gradient.

3.3.2 Sensor Thermal Model

Figure 3.5 shows the top view of the sensor schematic. In order to calculate the sensitivity of the gas sensor, the temperature distribution in the x-direction along the beam should be derived. Assume a uniform temperature distribution in the y-direction and a uniform thermal conductivity of the beam.

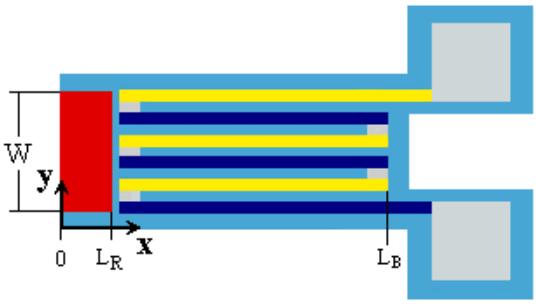

Figure 3.5: Top view of sensor schematic with resistor from $x = 0$ to $x = L_R$ and the beam from $x = L_R$ to $x = L_B$

3.3.2.1 Heat Radiation and Heat Conduction on Resistor

First of all, the heat transfer equations relevant to the resistor ($0 \leqslant x \leqslant L_R$) are derived:

Heat radiation P_{rad-r} from the resistor is given by

$$P_{rad-r} = \epsilon \cdot \sigma \cdot A_R \left(T_R^4 - T_a^4\right) \tag{3.7}$$

where the constant ε is the emissivity factor, σ is the Stefan–Boltzmann constant which equals to $5.67 \times 10^{-8}[\frac{\mathrm{W}}{\mathrm{m^2K^4}}]$, and A_R is the radiating resistor area, T_R is the temperature of the hot resistor, and T_a is the temperature of the heat sink (cold edge).

Heat conduction P_{cond-r} from the resistor to the heat sink through the gas path in z direction is given by

$$P_{cond-r} = \lambda_g \cdot \frac{1}{d} \cdot A_R \left(T_R - T_a\right) \tag{3.8}$$

where A_R is the resistor surface area which expressed as $A_R = W \cdot L_R.$, T_R is the temperature of the hot resistor, and T_a is the temperature of the heat sink (cold edge).

Since the temperature of the resistor is moderately higher than the temperature of the heat sink, which means

$$T_R > T_a > 0 \text{ and } \frac{T_R - T_a}{T_a} \ll 1, \tag{3.9}$$

$$\text{thus } 1 < \frac{T_R}{T_a} \ll 2, \text{ which means } \frac{T_R}{T_a} \approx 1 \tag{3.10}$$

Then heat radiation P_{rad-r} in equation 3.7 is expressed as

$$\begin{aligned} P_{rad-r} &= \epsilon \cdot \sigma \cdot A_R \cdot (T_R + T_a)\left(T_R^2 + T_a^2\right)(T_R - T_a) \\ &= \epsilon \cdot \sigma \cdot A_R \cdot T_a^3 \left(\frac{T_R}{T_a} + 1\right)\left[\left(\frac{T_R}{T_a}\right)^2 + 1\right](T_R - T_a) \qquad (3.11) \\ &\approx 4\epsilon \cdot \sigma \cdot A_R \cdot T_a^3 (T_R - T_a) \qquad (3.12) \end{aligned}$$

Thus, the heat power from the heater (resistor) to the beam is

$$\begin{aligned} P_{L_R} &= P_{in} - (P_{rad-r} + P_{cond-r}) \\ &= P_{in} - \left(4\epsilon \cdot \sigma \cdot T_a^3 + \lambda_g \cdot \frac{1}{d}\right)(T_R - T_a) A_R \qquad (3.13) \end{aligned}$$

3.3.2.2 Heat Flux through the Interface

Secondly, the heat flux through the interface on $x = L_R$ are conducted in two ways:

1. As states in the law of heat conduction, the heat flux expressed in equation 3.6 can be described as:

$$\phi_q = -\lambda \cdot \frac{dT(x)}{dx} \tag{3.14}$$

in which the thermal conductivity of the beam is expressed as

$$\lambda = \frac{\sum \lambda_s \cdot t_s}{\sum t_s} \tag{3.15}$$

with film thickness $t_s (s = 1, 2, ..)$ and thermal conductivities of films $\lambda_s (s = 1, 2, ..)$

2. By definition, the heat flux is the amount of energy that flows through a particular surface per unit area per unit time, which is described as:

$$\phi_q = \frac{P_{L_R}}{A_c} = \frac{P_{in} - \left(4\epsilon \cdot \sigma \cdot T_a^3 + \lambda_g \cdot \frac{1}{d}\right)(T_R - T_a) A_R}{A_c} \tag{3.16}$$

in which the cross section area $A_c = W\left(\sum t_s\right)$.

Combine the heat flux equation 3.14 and the equation 3.16, result in:

$$\phi_q = \frac{P_{in} - \left(4\epsilon \cdot \sigma \cdot T_a^3 + \lambda_g \cdot \frac{1}{d}\right)(T_R - T_a) A_R}{A_c} = -\left[\lambda \cdot \frac{dT(x)}{dx}\right] |_{x=L_R}$$

Apply $A_c = W\left(\sum t_s\right)$ and $\lambda = \frac{\sum \lambda_s \cdot t_s}{\sum t_s}$, and remove the term $\sum t_s$ on both sides, obtain this first-order differential equation:

$$\frac{dT(x)}{dx} |_{x=L_R} = -\frac{\frac{P_{in}}{W} - \left(4\epsilon \cdot \sigma \cdot T_a^3 + \lambda_g \cdot \frac{1}{d}\right)(T_R - T_a) L_R}{\sum \lambda_s \cdot t_s} \tag{3.17}$$

3.3.2.3 Heat Radiation and Heat Conduction on Beam

Thirdly, the heat transfer equations relevant to the beam ($L_R \leqslant x \leqslant L_B$) are derived:

Heat radiation P_{rad-b} from the resistor is given by

$$\begin{aligned} P_{rad-b} &= \epsilon \cdot \sigma \cdot A_b \left[T(x)^4 - T_a^4\right] \\ &\approx 4\epsilon \cdot \sigma \cdot A_b \cdot T_a^3 \left[T(x) - T_a\right] \end{aligned} \tag{3.18}$$

where the constant ε is the emissivity factor, σ is the Stefan–Boltzmann constant which equals to $5.67 \times 10^{-8}[\frac{\mathrm{W}}{\mathrm{m^2K^4}}]$, and A_R is the radiating beam area, $T(x)$ is the temperature at point x on the beam ($L_R \leqslant x \leqslant L_B$), and T_a is the temperature of the heat sink (cold edge).

Heat conduction P_{cond-b} from the resistor to the heat sink through the gas path in z direction is given by

$$P_{cond-b} = \lambda_g \cdot \frac{1}{d} \cdot A_b \left[T(x) - T_a\right] \tag{3.19}$$

where A_R is the resistor surface area which expressed as $A_R = W \cdot L_R$, T_R is the

temperature of the hot resistor, and T_a is the temperature of the heat sink.

3.3.2.4 Second-order Differential Heat Equation of Beam

Apply the heat equation 3.5 results in

$$\frac{d^2\left[T\left(x\right)-T_a\right]}{dx^2}+\frac{\Phi_s}{\lambda}=0 \tag{3.20}$$

in which T_a denoting the environmental temperature, Φ_s is the heat source power per volume V, and λ is the thermal conductivity.
With $V = A_b \cdot \sum t_s$, the power of heat source/loss of the beam per volume V is expressed by:

$$\begin{aligned}\Phi_s &= -\frac{P_{rad-b}+P_{cond-b}}{V}\\ &= -\frac{\left(4\epsilon\cdot\sigma\cdot T_a^3+\lambda_g\cdot\frac{1}{d}\right)\cdot A_b}{V}\left[T\left(x\right)-T_a\right]\\ &= -\frac{4\epsilon\cdot\sigma\cdot T_a^3+\lambda_g\cdot\frac{1}{d}}{\sum t_s}\left[T\left(x\right)-T_a\right]\end{aligned} \tag{3.21}$$

From $\lambda = \frac{\sum \lambda_s \cdot t_s}{\sum t_s}$, equation 3.20 and equation 3.21, the second-order differential equation is derived as:

$$\frac{d^2\left[T\left(x\right)-T_a\right]}{dx^2}-\frac{4\epsilon\cdot\sigma\cdot T_a^3+\lambda_g\cdot\frac{1}{d}}{\sum\lambda_s\cdot t_s}\left[T\left(x\right)-T_a\right]=0 \tag{3.22}$$

where ϵ denotes the emissivity of the cantilever material, σ is the Stefan-Boltzmann constant, A the beam surface area and x the variable distance along the beam.

Assume

$$C=\sqrt{\frac{4\epsilon\cdot\sigma\cdot T_a^3+\lambda_g\cdot\frac{1}{d}}{\sum\lambda_s\cdot t_s}} \tag{3.23}$$

then the equation 3.22 turns into

$$\frac{d^2\left[T\left(x\right)-T_a\right]}{dx^2}-C^2\left[T\left(x\right)-T_a\right]=0 \tag{3.24}$$

The general solution of the second-order differential equation 3.24 is given as:

$$T(x) - T_a = A \cdot e^{-Cx} + B \cdot e^{+Cx} \tag{3.25}$$

3.3.2.5 Boundary Conditions

Assume that a uniform temperature distribution in x-direction on the beam.

With L_B denoting the beam length, L_R the length of the heater (see Figure 3.5), the following boundary conditions apply:

1. heat-sink boundary condition:

$$T(L_B) = T_a \tag{3.26}$$

2. heat-source boundary condition:

$$T(L_R) = T_R \tag{3.27}$$

Apply the heat-sink condition into equation 3.26 into the general solution of the second-order differential equation 3.25, results in

$$\begin{aligned} & A \cdot e^{-CL_B} + B \cdot e^{+CL_B} = 0 \\ \Rightarrow \quad & A = -B \cdot e^{+2CL_B} \end{aligned} \tag{3.28}$$

Apply the heat-source condition equation 3.27 into the general solution of the second-order differential equation 3.25, results in

$$\begin{aligned} & A \cdot e^{-CL_R} + B \cdot e^{+CL_R} = T_R - T_a \\ \Rightarrow \quad & B \cdot \left[-e^{+C(2L_B - L_R)} + e^{+CL_R}\right] = T_R - T_a \end{aligned} \tag{3.29}$$

From equation 3.28 and equation 3.29, A and B is derived as

$$B = -\frac{T_R - T_a}{e^{+CL_B}\left[e^{+C(L_B - L_R)} - e^{-C(L_B - L_R)}\right]} \tag{3.30}$$

$$A = \frac{(T_R - T_a) \cdot e^{+2CL_B}}{e^{+CL_B}\left[e^{+C(L_B - L_R)} - e^{-C(L_B - L_R)}\right]} \tag{3.31}$$

Take A and B back into equation 3.25, the particular solution of the second-order differential equation 3.25 is

$$\begin{aligned} T(x) - T_a &= \frac{(T_R - T_a) \cdot e^{+2CL_B} \cdot e^{-Cx}}{e^{+CL_B}\left[e^{+C(L_B - L_R)} - e^{-C(L_B - L_R)}\right]} - \frac{(T_R - T_a) \cdot e^{+Cx}}{e^{+CL_B}\left[e^{+C(L_B - L_R)} - e^{-C(L_B - L_R)}\right]} \\ &= (T_R - T_a) \frac{e^{+C \cdot L_B} \cdot \left[e^{+C \cdot (L_B - x)} - e^{-C \cdot (L_B - x)}\right]}{e^{+C \cdot L_B} \cdot \left[e^{-C \cdot (L_B - L_R)} - e^{+C \cdot (L_B - L_R)}\right]} \\ &= (T_R - T_a) \frac{\sinh\left[C \cdot (L_B - x)\right]}{\sinh\left[C \cdot (L_B - L_R)\right]} \end{aligned} \tag{3.32}$$

then the temperature on the beam is

$$T(x) = (T_R - T_a) \frac{\sinh\left[C \cdot (L_B - x)\right]}{\sinh\left[C \cdot (L_B - L_R)\right]} + T_a \tag{3.33}$$

3.3.2.6 T_R Calculation

The expression for the temperature of the hot resistor T_R is derived as follows. Differential the equation 3.33, get

$$\begin{aligned} \frac{dT(x)}{dx} &= (T_R - T_a) \frac{d\left\{\frac{\sinh[C \cdot (L_B - x)]}{\sinh[C \cdot (L_B - L_R)]}\right\}}{dx} \\ &= (T_R - T_a) \frac{-C \cdot \cosh\left[C \cdot (L_B - x)\right]}{\sinh\left[C \cdot (L_B - L_R)\right]} \end{aligned} \tag{3.34}$$

Apply the equation 3.23, the differential equation 3.17 is expressed as:

$$\frac{dT(x)}{dx} \Big|_{x = L_R} = -\frac{\frac{P_{in}}{W} - C^2 \left(\sum \lambda_s \cdot t_s\right) (T_R - T_a) L_R}{\sum \lambda_s \cdot t_s} \tag{3.35}$$

Combine the equation 3.35 and equation 3.34, get

$$(T_R - T_a) \frac{C \cdot \cosh\left[C \cdot (L_B - L_R)\right]}{\sinh\left[C \cdot (L_B - L_R)\right]} = \frac{\frac{P_{in}}{W} - C^2 \left(\sum \lambda_s \cdot t_s\right) (T_R - T_a) L_R}{\sum \lambda_s \cdot t_s} \tag{3.36}$$

$$\text{thus } T_R = \frac{\frac{P_{in}}{C \cdot W \left(\sum \lambda_s \cdot t_s\right)}}{C \cdot L_R + \coth\left[C \cdot (L_B - L_R)\right]} + T_a \tag{3.37}$$

$$\text{in which } C = \sqrt{\frac{4\epsilon \cdot \sigma \cdot T_a^3 + \lambda_g \cdot \frac{1}{d}}{\sum \lambda_s \cdot t_s}} \tag{3.38}$$

3.3.3 Sensitivity

3.3.3.1 Sensitivity to Thermal Conductivity

The sensitivity of the sensor to the change in thermal conductivity is defined as the ratio of the change in the output Seebeck voltage $\Delta U_{seebeck}$ to the change in the thermal conductivity of gas $\Delta\lambda_g$ at a fixed input power, which is expressed by:

$$S = \frac{\Delta U_{seebeck}}{\Delta \lambda_g} \left[\frac{\text{mV} \cdot \text{m} \cdot \text{K}}{\text{W}}\right]$$

then C is the function of $\Delta\lambda_g$ which is expressed as

$$C\left(\Delta\lambda_g\right) = \sqrt{\frac{4\epsilon \cdot \sigma \cdot T_a^3 + \left[\Delta\lambda_g + \lambda_{air}\right] \cdot \frac{1}{d}}{\sum \lambda_s \cdot t_s}} \tag{3.39}$$

$$thus\ T_R\left(\Delta\lambda_g\right) = \frac{\frac{P_{in}}{C(\Delta\lambda_g) \cdot W(\sum \lambda_s \cdot t_s)}}{C\left(\Delta\lambda_g\right) \cdot L_R + \coth\left[C\left(\Delta\lambda_g\right) \cdot \left(L_B - L_R\right)\right]} + T_a$$

in the air, the thermal conductivity is $\lambda_g\left(0\right) = \lambda_{air}$, $\Delta\lambda_g = 0$. Consequently,

$$C_{air} = C\left(0\right) = \sqrt{\frac{4\epsilon \cdot \sigma \cdot T_a^3 + \lambda_{air} \cdot \frac{1}{d}}{\sum \lambda_s \cdot t_s}} \tag{3.40}$$

$$\text{and } T_R\left(0\right) = \frac{\frac{P_{in}}{C(0) \cdot W(\sum \lambda_s \cdot t_s)}}{C\left(0\right) \cdot L_R + \coth\left[C\left(0\right) \cdot \left(L_B - L_R\right)\right]} + T_a$$

The Seebeck voltage is

$$U_{seebeck} = \alpha \cdot n_t \left(T_R - T_a\right) \tag{3.41}$$

Thus the sensitivity is expressed as

$$S = \left| \frac{U_{seebeck-gas} - U_{seebeck-air}}{\Delta\lambda_g} \right| \tag{3.42}$$

$$= \left| \frac{\alpha \cdot n_t \left\{ \left[T_R \left(\Delta\lambda_g \right) - T_a \right] - \left[T_R \left(0 \right) - T_a \right] \right\}}{\Delta\lambda_g} \right| \tag{3.43}$$

$$\left| \frac{\alpha \cdot n_t \left[T_R \left(\Delta\lambda_g \right) - T_R \left(0 \right) \right]}{\Delta\lambda_g} \right| \tag{3.44}$$

$$\text{in which } T_R \left(\Delta\lambda_g \right) = \frac{\frac{P_{in}}{C(\Delta\lambda_g) \cdot W(\sum \lambda_s \cdot t_s)}}{C \left(\Delta\lambda_g \right) \cdot L_R + \coth \left[C \left(\Delta\lambda_g \right) \cdot \left(L_B - L_R \right) \right]} + T_a$$

$$\text{and } C \left(\Delta\lambda_g \right) = \sqrt{\frac{4\epsilon \cdot \sigma \cdot T_a^3 + \left[\Delta\lambda_g + \lambda_{air} \right] \cdot \frac{1}{d}}{\sum \lambda_s \cdot t_s}} \tag{3.45}$$

3.3.3.2 Sensitivity to Measurand Gas Concentration

At a given input power, the sensor sensitivity is defined as the ratio of the change in output Seebeck voltage to the change in the measurand gas concentration in air. Assume the change in the measurand gas concentration in air is α, the sensor sensitivity is expressed by:

$$S = \frac{\Delta U_{seebeck}}{\alpha} \text{ [mV]}$$

assume the concentration of measurand gas change rate is k, then the thermal conductivity of the gas is expressed by:

$$\lambda_g \left(k \right) = k \cdot \lambda_{mea} + \left(1 - k \right) \cdot \lambda_{air}$$

then C is the function of k as

$$C \left(k \right) = \sqrt{\frac{4\epsilon \cdot \sigma \cdot T_a^3 + \left[k \cdot \lambda_{mea} + \left(1 - k \right) \cdot \lambda_{air} \right] \cdot \frac{1}{d}}{\sum \lambda_s \cdot t_s}} \tag{3.46}$$

$$\text{thus } T_R \left(k \right) = \frac{\frac{P_{in}}{C(k) \cdot W(\sum \lambda_s \cdot t_s)}}{C \left(k \right) \cdot L_R + \coth \left[C \left(k \right) \cdot \left(L_B - L_R \right) \right]} + T_a$$

the thermal conductivity in air is $\lambda_g \left(0 \right) = \lambda_{air}$, $k = 0$. Consequently,

$$C_{air} = C \left(0 \right) = \sqrt{\frac{4\epsilon \cdot \sigma \cdot T_a^3 + \lambda_{air} \cdot \frac{1}{d}}{\sum \lambda_s \cdot t_s}} \tag{3.47}$$

$$\text{and } T_R(0) = \frac{\frac{P_{in}}{C(0)\cdot W(\sum \lambda_s \cdot t_s)}}{C(0)\cdot L_R + \coth\left[C(0)\cdot(L_B - L_R)\right]} + T_a$$

When the thermal conductivity of the measurand gas is smaller than air, for instance CO_2, the thermal conductivity of the mixture-gas is

$$\lambda_g = k\lambda_{mea} + (1-k)\,\lambda_{air} < \lambda_{air}$$

and the output Seebeck Voltage is larger than that in air as

$$U_{seebeck-gas} > U_{seebeck-air}$$

when the thermal conductivity of the measurand gas is larger than air, for instance H_2, the thermal conductivity of the mixture-gas is

$$\lambda_g = k\lambda_{mea} + (1-k)\,\lambda_{air} > \lambda_{air}$$

and the output Seebeck Voltage is larger than that in air as

$$U_{seebeck-gas} < U_{seebeck-air}$$

The Seebeck voltage is expressed as

$$U_{seebeck} = \alpha \cdot n_t\,(T_R - T_a) \tag{3.48}$$

Thus the sensitivity is expressed as

$$S = \left| \frac{\alpha \cdot n_t\left[T_R(k) - T_R(0)\right]}{k} \right| \tag{3.49}$$

$$\text{in which} \quad T_R(k) = \frac{\frac{P_{in}}{C(k)\cdot W(\sum \lambda_s \cdot t_s)}}{C(k)\cdot L_R + \coth\left[C(k)\cdot(L_B - L_R)\right]} + T_a \tag{3.50}$$

$$\text{and } C(k) = \sqrt{\frac{4\epsilon\cdot\sigma\cdot T_a^3 + \left[k\cdot\lambda_{mea} + (1-k)\cdot\lambda_{air}\right]\cdot\frac{1}{d}}{\sum \lambda_s \cdot t_s}} \tag{3.51}$$

3.4 Sensor Sensitivity Optimization

The analytical analysis of sensor sensitivity is based on Matlab software simulation.

The following simulations are based on **detecting the change in output Seebeck voltage with an increase in the hydrogen concentration in air from 0% to 3% with 1.2mW input power**.

The specifications of the simulated sensor structure is shown in Figure 3.6. The number of thermocouples n_t is 10, the beam width W is 154μm, the beam length L_B is 100μm, and the gas path d is 4μm.

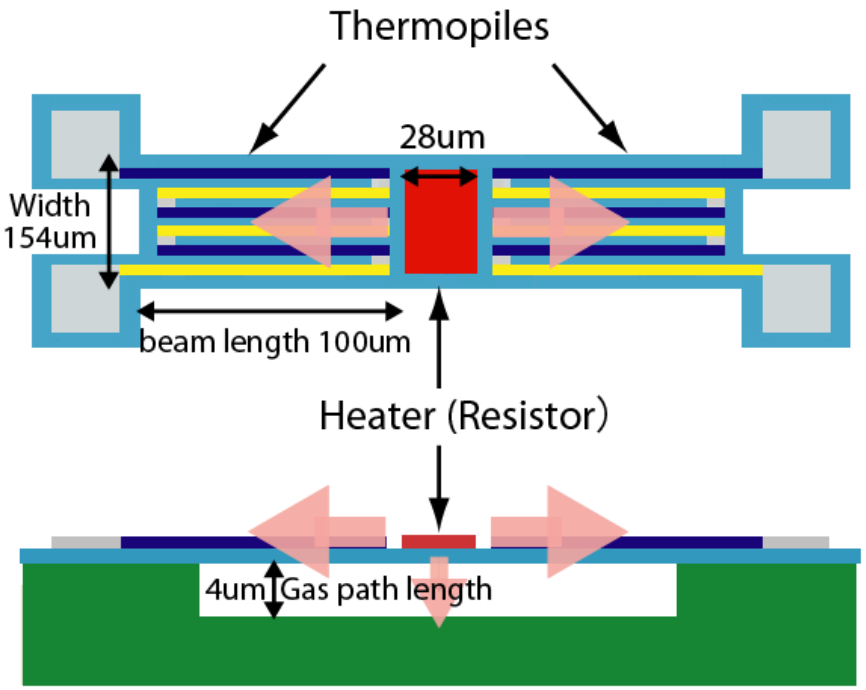

Figure 3.6: Specifications of the simulated sensor structure

3.4.1 Radiation Effects

The radiation effects can be neglected due to the radiation is extremely small compared with the conduction in the temperature range of the hot resistor which is lower than 400K.

When the resistor temperature is 636.8K, the radiation $P_{rad-r} = \epsilon \cdot \sigma \cdot A_R \left(T_R^4 - T_a^4\right)$ is still only 0.1% of the conduction $P_{cond-r} = \lambda_g \cdot \frac{1}{d} \cdot A_R \left(T_R - T_a\right)$.

Consequently, the term $4\epsilon \cdot \sigma \cdot T_a^3$ in $C = \sqrt{\frac{4\epsilon \cdot \sigma \cdot T_a^3 + \lambda_g \cdot \frac{1}{d}}{\sum \lambda_s \cdot t_s}}$ can be **neglected at temperature below 636.8K**, since they result in an error much less than 0.1%.

Thus the sensitivity is expressed by,

$$S = \mid \frac{\alpha \cdot n_t \left[T_R(k) - T_R(0)\right]}{k} \mid \tag{3.52}$$

$$\text{in which} \quad T_R(k) = \frac{\frac{P_{in}}{C(k) \cdot W(\sum \lambda_s \cdot t_s)}}{C(k) \cdot L_R + \coth\left[C(k) \cdot (L_B - L_R)\right]} + T_a \tag{3.53}$$

$$C(k) = \sqrt{\frac{\left[k \cdot \lambda_{mea} + (1-k) \cdot \lambda_{air}\right] \cdot \frac{1}{d}}{\sum \lambda_s \cdot t_s}} \tag{3.54}$$

3.4.2 Input Power

The sensitivity as a function of the input power is expressed as

$$S(P_{in}) = P_{in} \mid \frac{\frac{\alpha \cdot n_t}{W(\sum \lambda_s \cdot t_s)} \left[\frac{\frac{1}{C(k)}}{C(k) \cdot L_R + \coth[C(k) \cdot (L_B - L_R)]} - \frac{\frac{1}{C(0)}}{C(0) \cdot L_R + \coth[C(0) \cdot (L_B - L_R)]}\right]}{k} \mid$$

$$\text{in which} \quad C(k) = \sqrt{\frac{\left[k \cdot \lambda_{H_2} + (1-k) \cdot \lambda_{air}\right] \cdot \frac{1}{d}}{\sum \lambda_s \cdot t_s}}$$

Seebeck coefficient α is 290 μV/K, the number of thermocouples n_t is 10, the beam width W is 154μm, the beam length L_B is 100μm, the gas path d is 4μm, the hydrogen concentration in air k is 3%.

Figure 3.7 shows the relationship between the sensitivity and the input power.

The sensitivity is proportional to the input power.

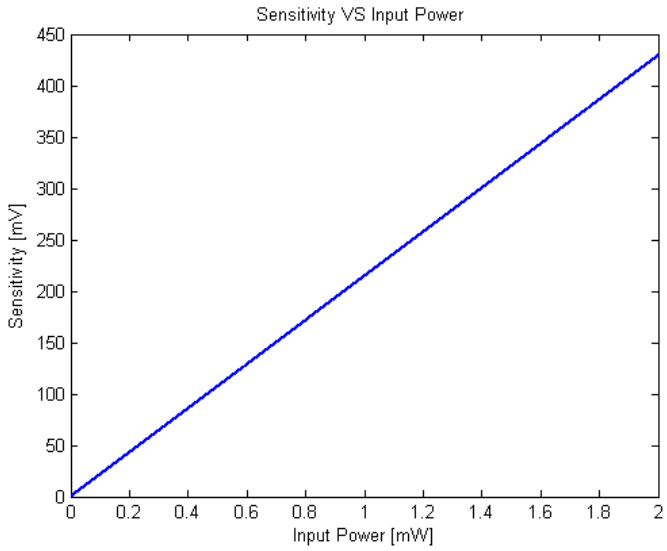

Figure 3.7: Sensitivity versus input power

3.4.3 Gas Path Length and Beam Length

The sensitivity as a function of the gas path length and beam length is expressed as

$$S\left(L_B,\, d\right) = \left| \frac{\frac{P_{in}\cdot\alpha\cdot n_t}{W(\sum\lambda_s\cdot t_s)}\left[\frac{\frac{1}{C1(d)}}{C1(d)\cdot L_R+\coth[C1(d)\cdot(L_B-L_R)]}-\frac{\frac{1}{C2(d)}}{C2(d)\cdot L_R+\coth[C2(d)\cdot(L_B-L_R)]}\right]}{k} \right|$$

$$\text{in which } \; C1\left(d\right)=\sqrt{\frac{\left[k\cdot\lambda_{H_2}+(1-k)\cdot\lambda_{air}\right]\cdot\frac{1}{d}}{\sum\lambda_s\cdot t_s}} \text{ and } C2\left(d\right)=\sqrt{\frac{\lambda_{air}\cdot\frac{1}{d}}{\sum\lambda_s\cdot t_s}}$$

Seebeck coefficient α is 290 μV/K, the number of thermocouples n_t is 10, the beam width W is 154μm, the beam length L_B is 100μm, the hydrogen concentration in air k is 3%.

Figure 3.8 shows the 3-dimensions plot of the sensitivity changes with the beam length (range: 30μm - 500μm) and the gas path length (range: 1μm - 50μm) . It can be seen that the sensitivity gets its maximum value when the gas path length is 50 μm and the beam length is more than 300μm.

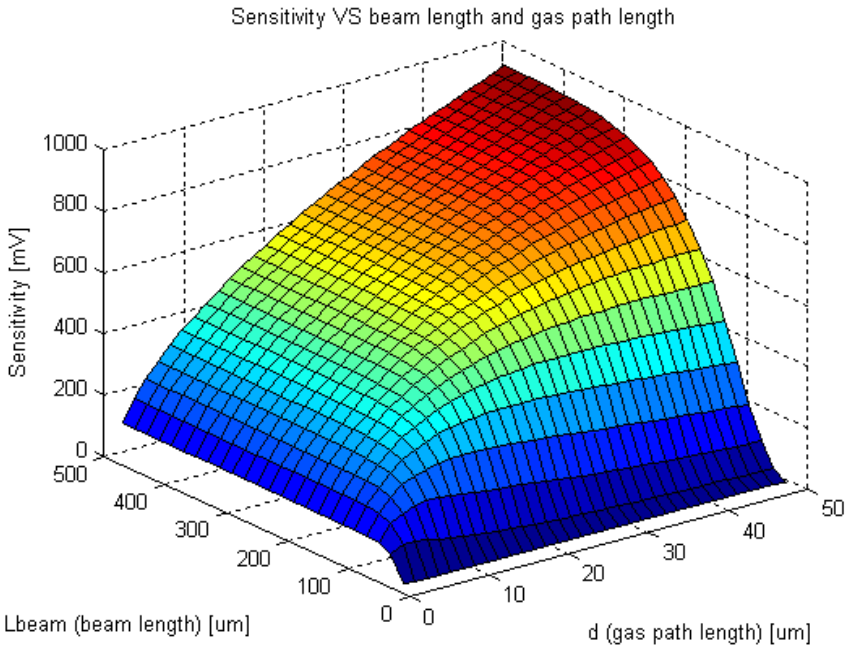

Figure 3.8: 3D plot of sensitivity versus beam length and gas path length

Figure 3.9 shows the corresponding sensitivity when the beam length is $1\mu m$, $5\mu m$, $10\mu m$, $20\mu m$, $50\mu m$, respectively.

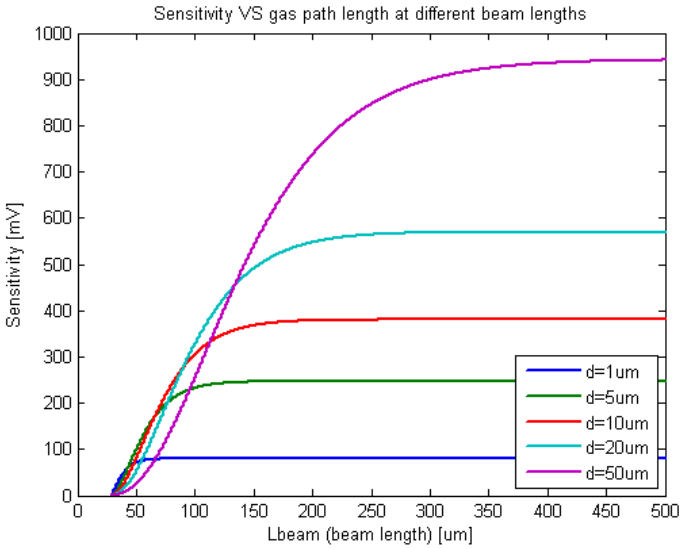

Figure 3.9: Sensitivity versus beam length at different gas path lengths

When the gas path length is $1\mu m$, the corresponding sensitivity gets its maximum value when the beam length is around $50\mu m$.
When the gas path length is $20\mu m$, the corresponding sensitivity gets its maximum value when the beam length is around $280\mu m$.

Figure 3.10 shows the 3-dimensions plot of the sensitivity changes with the gas path length (range: $0.1\mu m$ - $50\mu m$) and the beam length (range: $40\mu m$ - $500\mu m$).

It can be seen that the sensitivity gets its maximum value when the gas path length is 50 μm and the beam length is more than $300\mu m$.

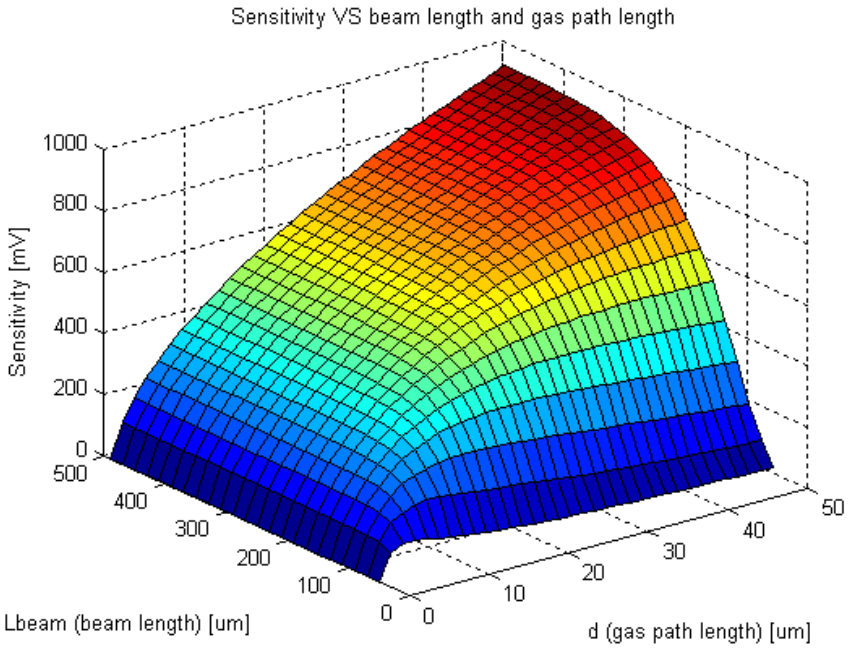

Figure 3.10: 3D plot of sensitivity versus beam length and gas path length

Figure 3.11 shows the corresponding sensitivity when the beam length is $50\mu m$, $100\mu m$, $150\mu m$, $200\mu m$, $250\mu m$, respectively.

When the beam length is $100\mu m$, the corresponding sensitivity gets its maximum value when the gas path length is around $20\mu m$.
When the beam length is $150\mu m$, the corresponding sensitivity gets its maximum value when the gas path length is around $50\mu m$.

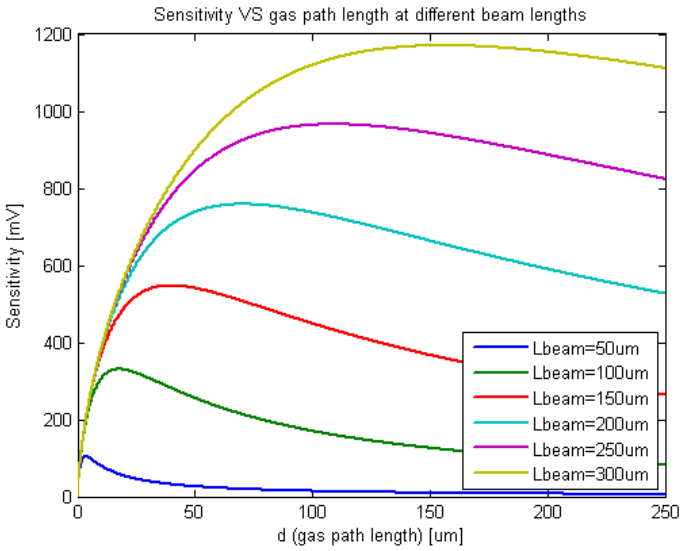

Figure 3.11: Sensitivity versus gas path length at different beam lengths

There is a optimum value of the gas path length for each beam length. The reasons why the sensor sensitivity is rather low when the gas path length is much shorter or longer than the optimum value are explained as follows.

When the gas path length is rather short, the temperature of heater is greatly influenced by the underneath cold substrate, which result in a low sensitivity to the changes in the thermal conductivity of measurand gas.

When the gas path length is rather long, as described in equation 2.1, **less heat from the heater will conducted through the gas, and more heat will lost through the beam, thus the temperature of heater has a lower sensitivity to the changes in the thermal conductivity of measurand gas.**

Consider the limitation of the fabrication process, a optimal sensor sensitivity of **568.8** mV is obtained for 1.2mW input power hydrogen detection with beam length 280μm and gas path length 20 μm.

3.5 Conclusions

- The thermal conductivity gas sensors perform a measurement of the thermal conductivity of measurand gas. By feeding current into the resistor in the center of the sensor, the resistor is heated up and becomes a "hot element". Then, the measurand gas transfers a quantity of heat from the hot resistor to the cold edge via thermal conduction through the measured gas, which leads to a decrease in the temperature of resistor. Thus, for a given experimental configuration and a fixed input power, **the changes in the thermal conductivity of measurand gas can be detected by measuring the changes in the temperature of resistor.**

- In order to **improve the sensor sensitivity by minimizing the heat loss to the suspended membrane** without any complex fabrication steps, **a simple floating membrane structured micro-thermoelectric gas sensor is fabricated using surface micromachining**.

- Consider the limitation of the fabrication process, a optimal sensor sensitivity of **568.8** mV is obtained for 1.2mW input power hydrogen detection with beam length $280\mu m$ and gas path length 20 μm using Matlab.

- The thermal modeling shows that **there is a optimum value of the gas path length for each beam length.**
  When the gas path length is rather short, the temperature of heater is greatly influenced by the underneath cold substrate, which result in a low sensitivity to the changes in the thermal conductivity of measurand gas.
  When the gas path length is rather long, less heat from the heater will conducted through the gas, and more heat will lost through the beam, thus the temperature of heater has a lower sensitivity to the changes in the thermal conductivity of measurand gas.

- **The radiation effects can be neglected at temperature below 636.8K,** since the radiation is less than 0.1% of the conduction and consequently result

in an error less than 0.1%.

Chapter 4

Sensor Design Based on Numerical Analysis

In this chapter, the sensor design based on numerical analysis will be presented. Firstly, the sensor will be modelled based on the finite element method (FEM) simulation using COMSOL Multiphysics software. Two application modes - the conductive media DC and heat transfer modules are combined into a single model for interaction simulation using the multiphysics features of COMSOL Multiphysics. Then, the relationship between sensor sensitivity and different features of sensor will be derived based on numerical simulations in COMSOL. Finally, the optimal sensor sensitivity will be obtained based on the simulation results in COMSOL.

4.1 Numerical Analysis

4.1.1 Coupled Modules for Interaction Simulation in COMSOL Multiphysics

In this gas sensor, the resistor coverts the input electrical power into heat power which leads to hot temperature, meanwhile the resistivity of the resistor varies with temperature. Consequently, this modeling need to include the interaction between thermal domain and electrical domain. To solve such problem, instead of conventionally using only one Heat Transfer module, t**wo application modes - the**

Conductive Media DC and Heat Transfer modules are combined into a single model using the multiphysics features of COMSOL Multiphysics. In this way, a system of two partial differential equations (PDE) with two dependent variables - V for the electric potential and T for the temperature - is created. This coupling occurs in subdomains and on boundaries.

4.1.2 Simplified Equivalent Model

The specifications of the simulated sensor structure are shown in Figure 4.1.

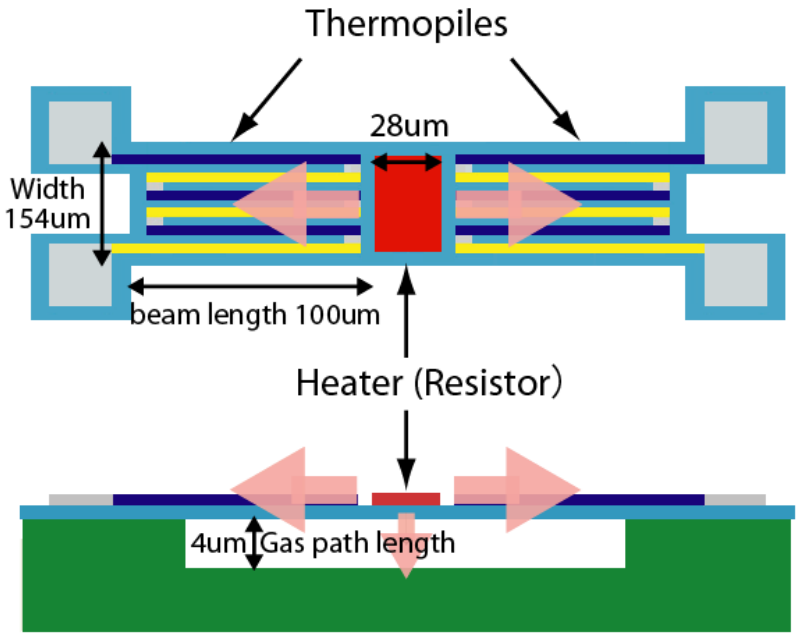

Figure 4.1: Structure and specifications of the simulated sensor

The temperature distribution of this gas sensor and the detailed gas sensor model which consists the layers stack in the beam are shown in Fig 4.2. The stack of different layers is represented by different colors. The light blue blocks represent the measurand gas, the red blocks stand for the P-type poly-silicon layer, the dark green blocks express the N-type poly-silicon layer, and the light green blocks are the silicon nitride.

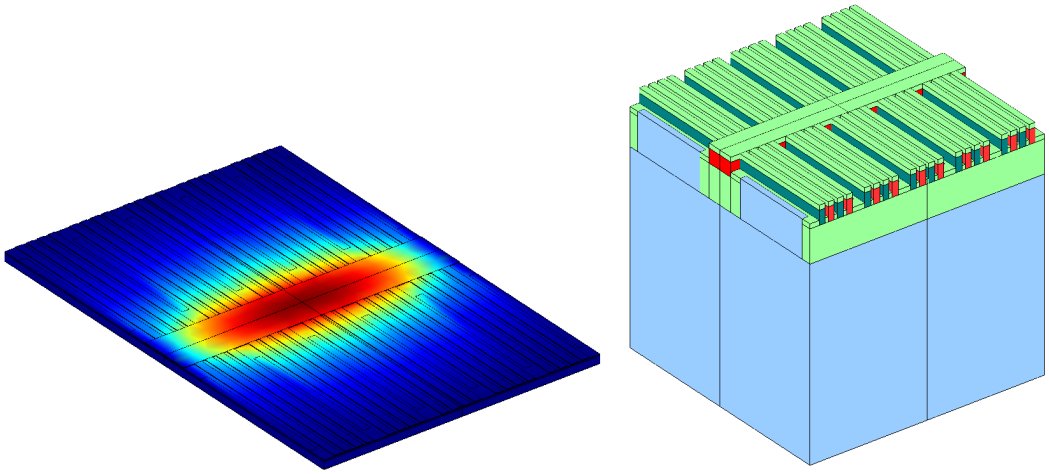

(a) temperature distribution (b) different layers

Figure 4.2: Detailed gas sensor model in COMSOL

Due to the complexity of the thermo-electric interactions system based on coupling two partial differential equations, the high precision in FEM model simulation, and the limitation of the random access memory of CPU, the detailed layers stack beam gas sensor model needs to be simplified. Equivalent thermal sensor model with equivalent beams which have equivalent thermal conductivity and equivalent thickness, as shown in Fig 4.3, simplify the detailed layers stack in the beam.

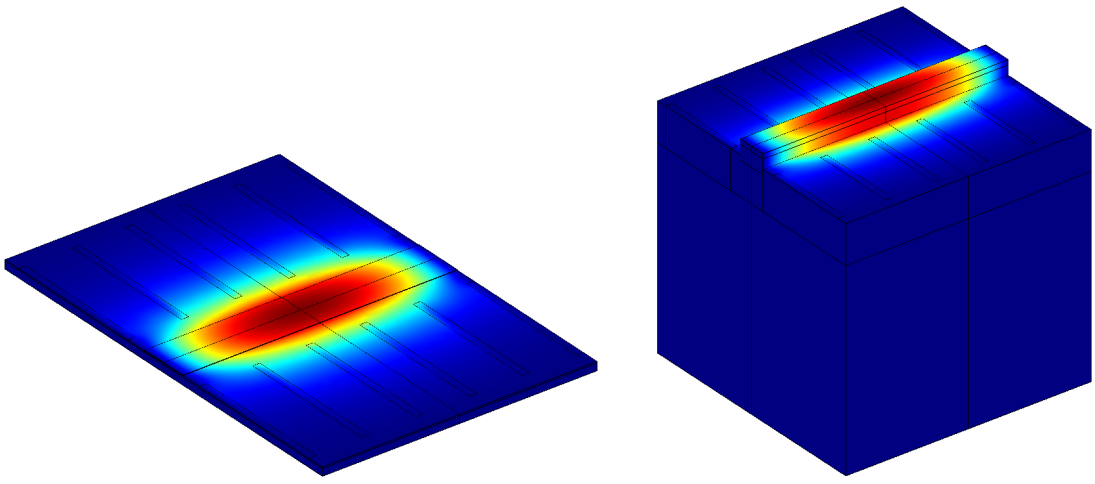

(a) temperature distribution (b) layer stack

Figure 4.3: Temperature distribution of simplified gas sensor model with equivalent beams in COMSOL

The resulting temperature difference is in direct ratio to the applied different values of heat source density into the resistor in the simplified model, as shown in Fig 4.4.

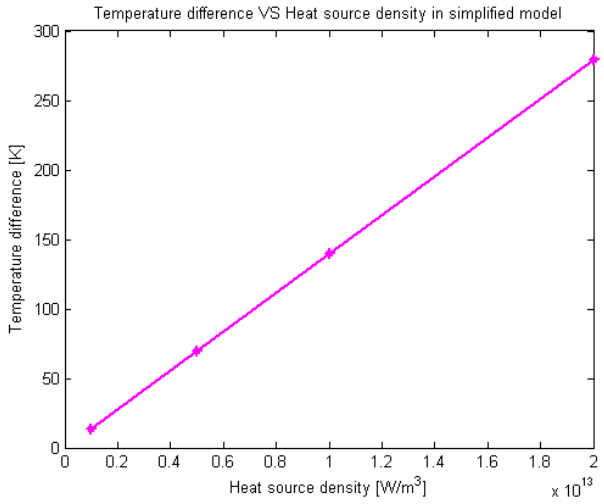

Figure 4.4: Temperature difference versus heat source density in simplified model

Fig 4.5 shows the deviation between original model and simplified model. The simplified model can replace the original model since it results in **an error less than 0.064%.**

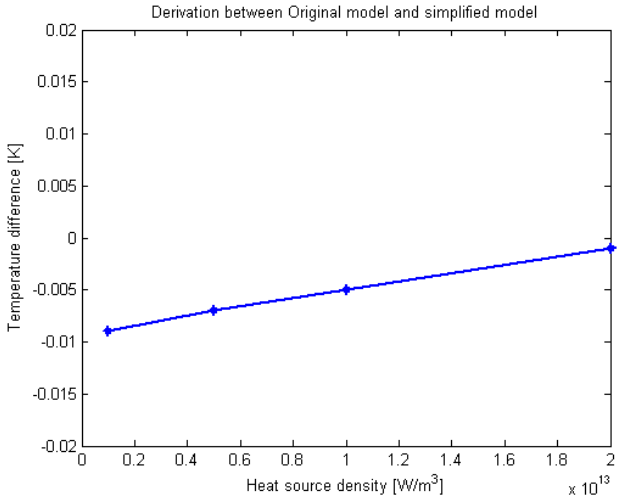

Figure 4.5: Derivation between original model and simplified model

4.1.3 Simulation of Detailed Resistor Model

The detailed meandered shape resistor is added into the simplified model in COMSOL as shown in Fig 4.6. The light blue blocks represent the measurand gas, the red blocks stand for the P-type poly-silicon layer, the pink blocks express the the equivalent beam layer, and the light green blocks are the silicon nitride.

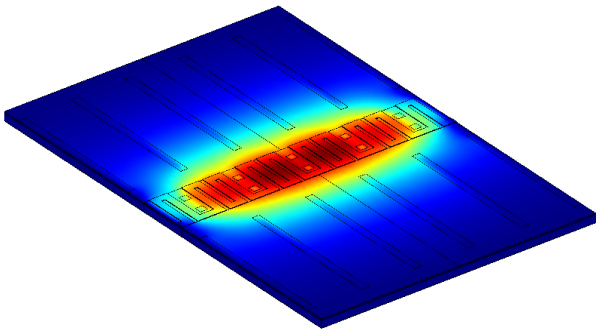

(a) temperature distribution

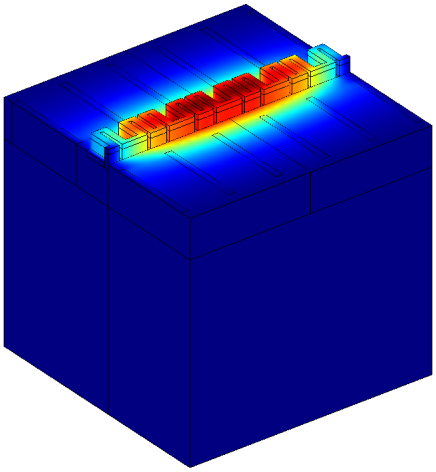

(b) layer stack

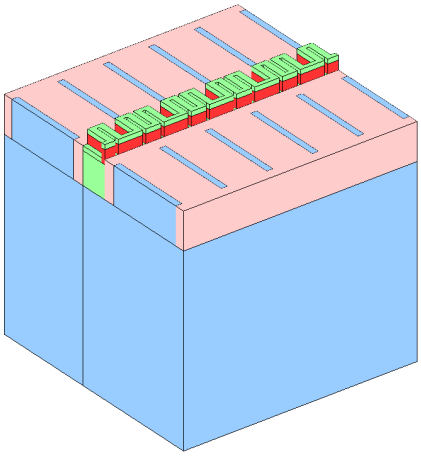

(c) different layers

Figure 4.6: Simplified model with detailed resistor

The simulation is based on joule-heating principle to express electro-thermal interaction by combining two application modes - the Conductive Media DC and Heat Transfer modules in COMSOL Multiphysics.

Apply the resistivity of the resistor as 4.5e-5[ohm*m], and temperature coefficient as 0.0008[1/K], T_0 as 300K. Apply 0.2mA current (1.66667e8 $^{A}/_{m^2}$ current density,

1.2e-12m^2 area) into the resistor.

The corresponding sensor temperature distribution and sensor electric potential distribution are shown in Figure 4.7 and Figure 4.8.

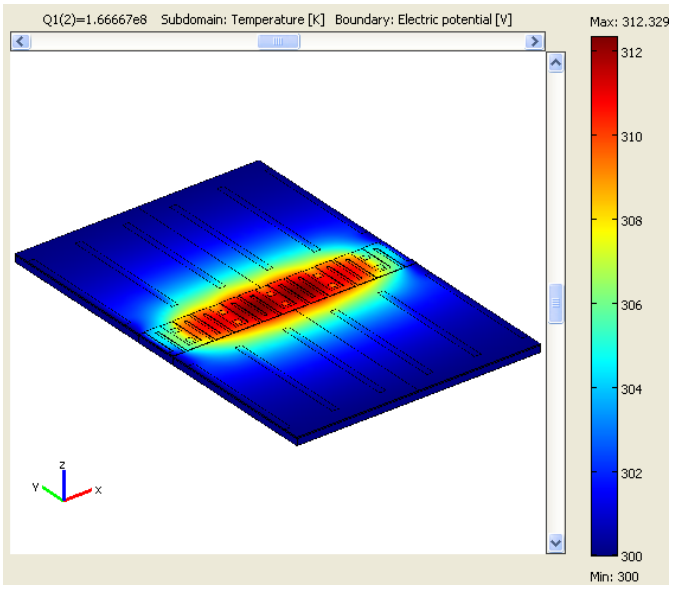

Figure 4.7: Electro-thermal interaction simulation: sensor temperature distribution

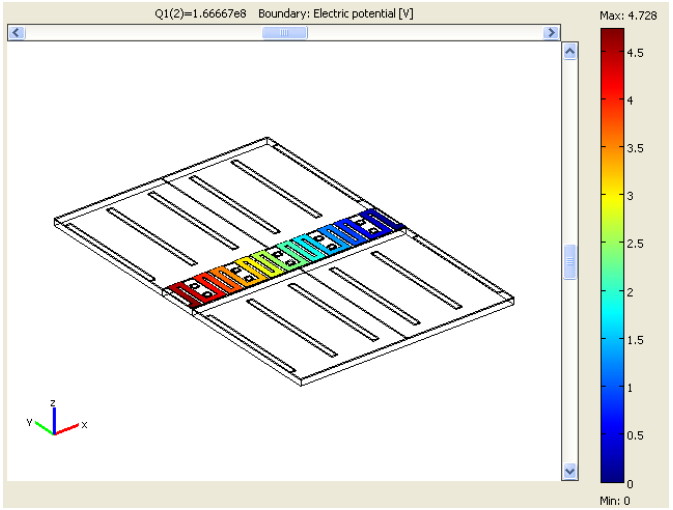

Figure 4.8: Electro-thermal interaction simulation: sensor electric potential distribution

4.1.3.1 Simulation Results

This simulation as shown in Figure 4.9 is based on detecting the change in output Seebeck voltage with an increase in the hydrogen concentration in air from 0% to 3% with different input power. The output Seebeck voltage is obtained precisely by averaging the temperature difference of all the thermocouples.

The results clearly shows that the output Seebeck voltage changes with the hydrogen concentration in air. **An increase in the hydrogen concentration in air from 0% to 3% leads to a decrease in the output Seebeck voltage of 1.42 mV at 1.2 mW input powers.**

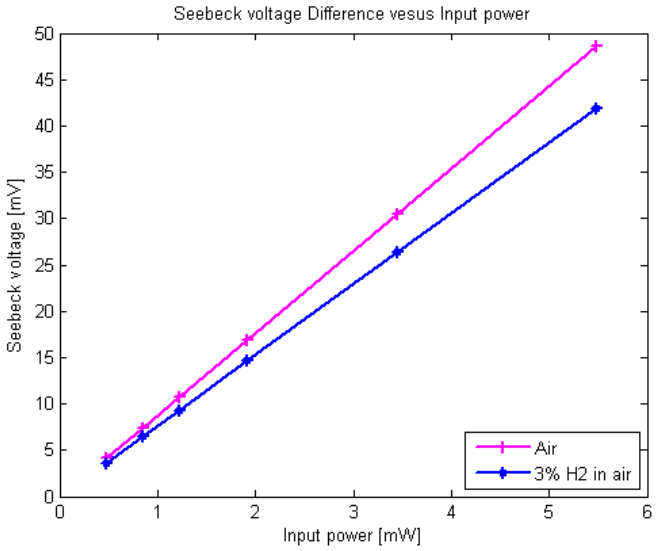

Figure 4.9: COMSOL simulation results for hydrogen detection

4.1.3.2 Heater Temperature Distribution

As shown in Figure 4.10, the temperature of the resistor is not homogeneously distributed. The reason is that the temperatures **at the two short ends of the resistor are significantly influenced by the cold edges.** The small drops on the curve are due to the periodical at the sensor structure.

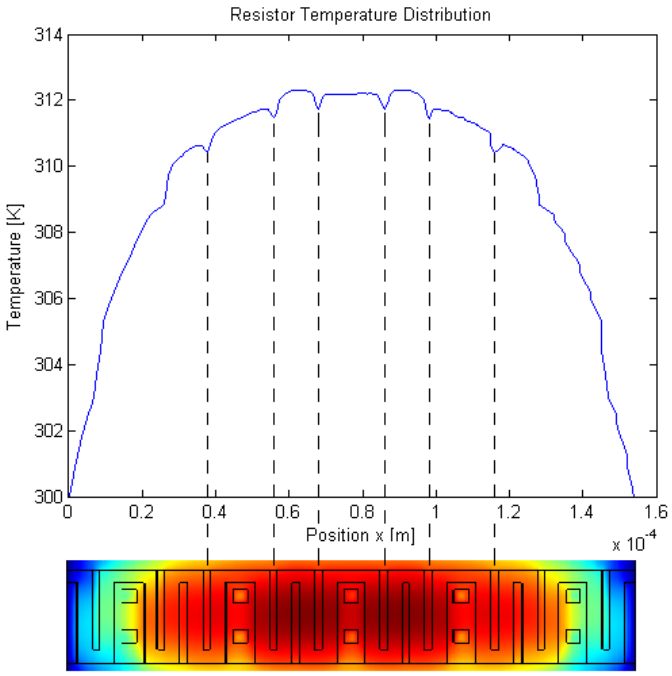

Figure 4.10: temperature distribution of the resistor.

4.1.4 Sensor Sensitivity Optimization

The numerical analysis of sensor sensitivity is based on COMSOL multiphysics software simulation. The following simulations are based on **detecting the change in output Seebeck voltage with an increase in the hydrogen concentration in air from 0% to 3% with 1.2mW input power.** The output Seebeck voltage is obtained precisely by averaging the temperature difference of all the thermocouples.

4.1.4.1 Single-Clamped Bridge

As shown in Figure 4.11, an improved sensor based on a single-clamped bridge is adopted instead of double-clamped structure, while larger gas opening are placed on the other side.

The light blue blocks represent the measurand gas, the pink blocks express the the equivalent beam layer, and the light green blocks are the silicon nitride.

The larger gas openings allows **the detected gas to flow in the chamber underneath the sensor more easily and decrease the heat loss through the beam**,

consequently, increase the sensitivity of the sensor by **58.27%** (from 132.5944573 mV to 209.852265 mV) .

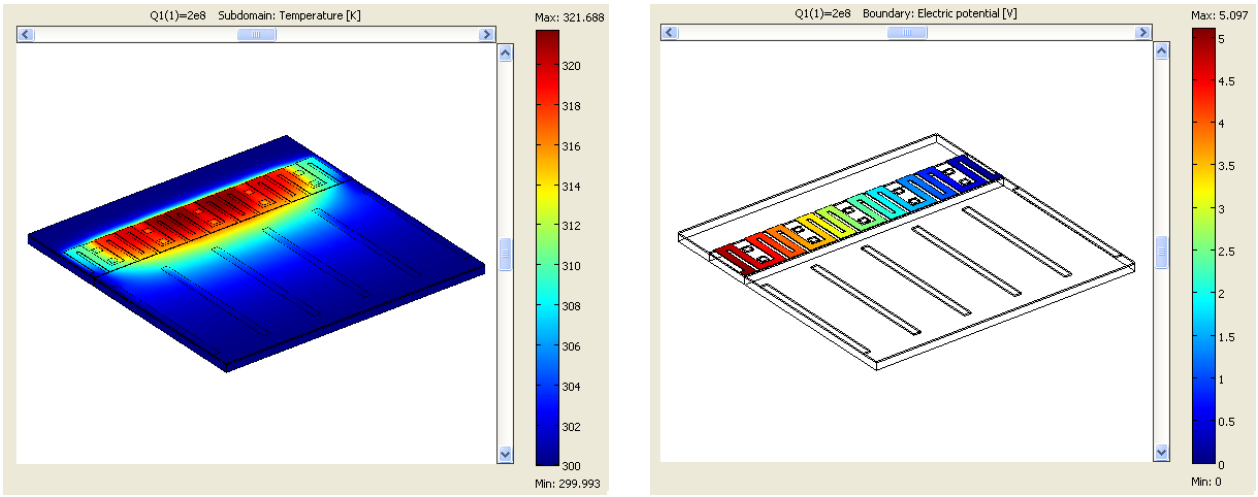

(a) temperature distribution

(b) electric potential distribution

(c) different layers

Figure 4.11: Improved sensor based on a single-clamped bridge

4.1.4.2 Number of Thermocouples

The relationship between the sensitivity and the number of thermocouples is obtained in the following simulations. Figure 4.12 shows the simulated gas sensors with 8, 10, 12, 16 pairs of thermocouples, respectively. In order to achieve a low noise and consequently a high detection limit in this sensor system, the resistance of the beam are recommended to be less than $200k\Omega$, thus the number of thermocouples should be less than sixteen.

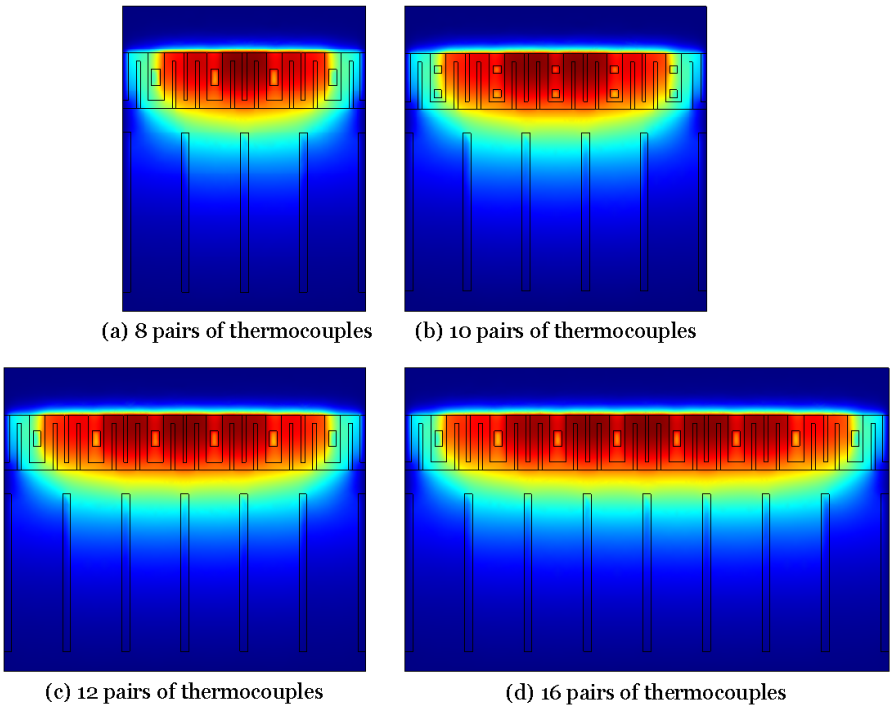

Figure 4.12: Simulated gas sensors with 8, 10, 12, 16 pairs of thermocouples

The relationship between the sensitivity and the number of thermocouples is shown in Figure 4.13.

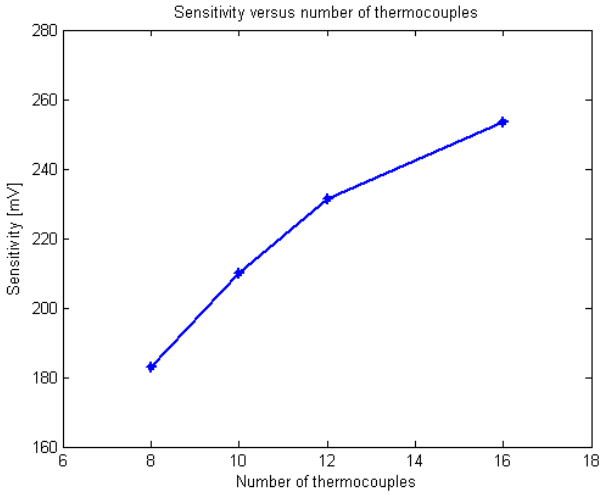

Figure 4.13: Sensitivity versus number of thermocouples

It is obvious that the sensor sensitivity increases with the number of ther-

mocouples. Consequently, sixteen pairs of thermocouples is the optimal value, while the sensitivity increases by **91.29%** (from 132.5944573 mV to 253.6427967 mV).

4.1.4.3 Beam Length

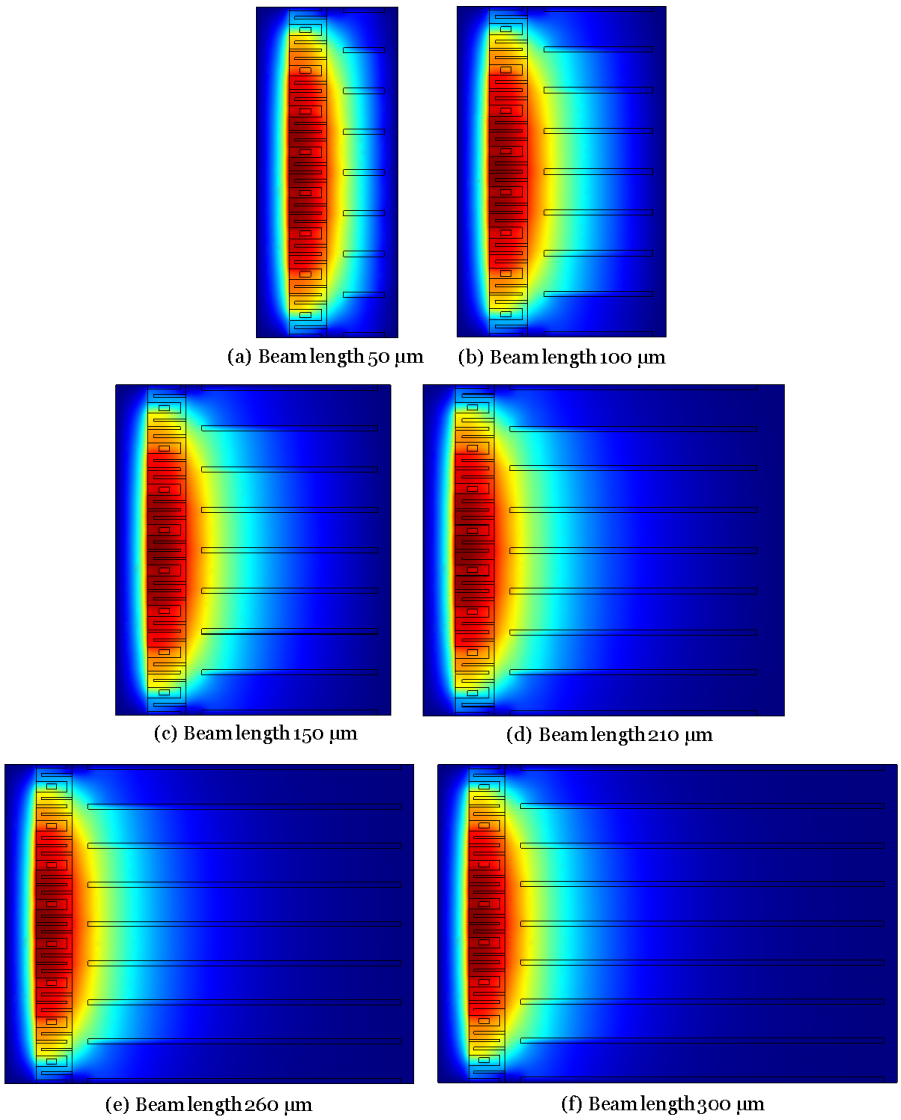

Figure 4.14: Simulated gas sensors with beam length of $50\mu m$, $100\mu m$, $150\mu m$, $210\mu m$, $260\mu m$, $300\mu m$

The relationship between the sensitivity and the beam length is obtained in the

following simulations. Consider the limitation of the fabrication process, the gas path length should be less than 20 μm. Consequently, the simulated gas sensors in Figure 4.14 are all with gas path length of 20 μm and with beam length of 50μm, 100μm, 150μm, 210μm, 260μm, 300μm, respectively.

The relationship between the sensitivity and the beam length is shown in Figure 4.15. **It is obvious that the sensor sensitivity increases with the beam length and will be saturated at optimal beam length** around 260μm**.**

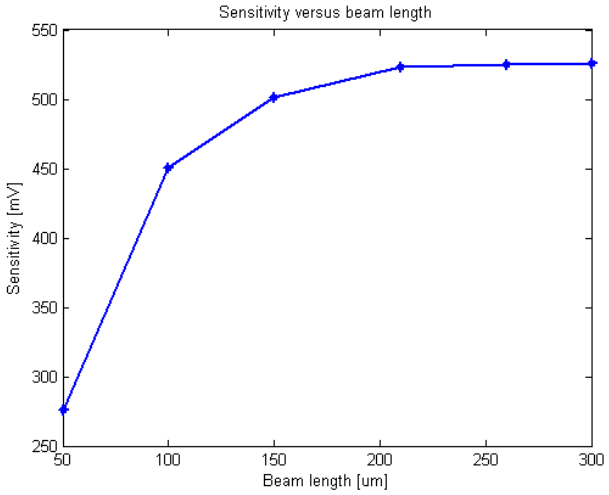

Figure 4.15: Sensitivity versus beam length

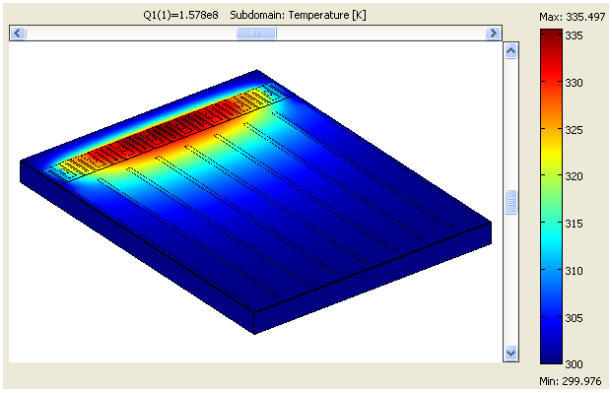

(a) temperature distribution

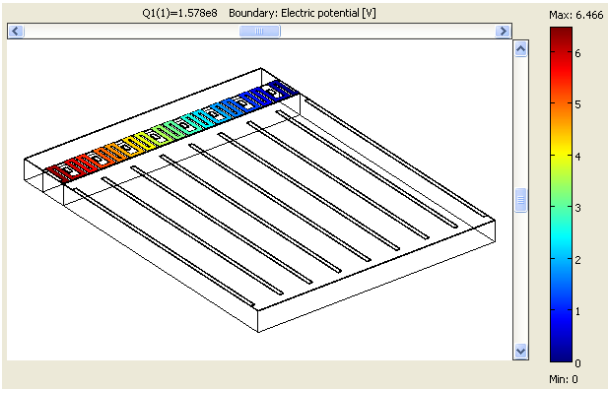

(b) electric potential distribution

Figure 4.16: Improved sensor with beam length 260μm and gas path length 20μm

On the other hand, in order to achieve a low noise and consequently a high detection limit in this sensor system, the resistance of the beam are recommended to be less than $200k\Omega$, thus the beam length should less than $260\mu m$. Consequently, the sensor with beam length $260\mu m$ and gas path length $20\mu m$ as shown in Figure 4.16 is the optimal structure, while its **sensitivity increases by 3.96 times** (from 132.5944573 mV to 524.967744 mV).

Compared with the analytical analysis

The corresponding analytical simulation is shown in Figure 4.17, it is obvious that **the sensor sensitivity increases with the beam length and will be saturated at optimal beam length** around $260\mu m$. This means **the numerical COMSOL simulation results show the same trend of the analytical simulation results** in Matlab Software.

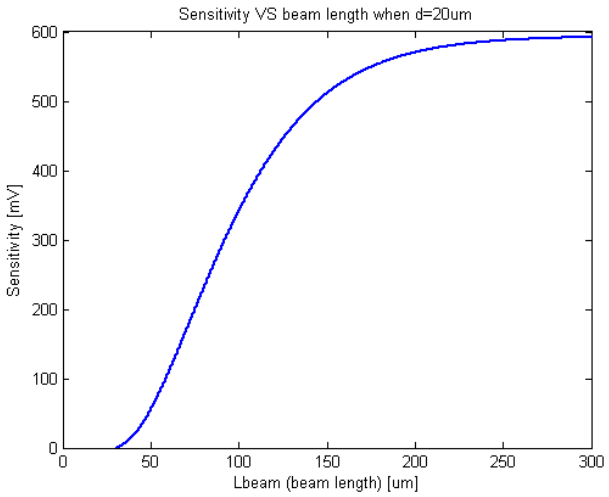

Figure 4.17: Sensitivity versus beam length - **analytical simulation**

4.1.4.4 Gas Path Length

The relationship between the sensitivity and the gas path length is obtained in the following simulations. As explained in section 4.1.4.3 above, the sensor beam length of $260\mu m$ is a optimal value when its gas path length $20\mu m$. Consequently, The simulated gas sensors in Figure 4.18 are all with beam length of $260\mu m$ and with gas path length of $1\mu m$, $4\mu m$, $10\mu m$, $20\mu m$, $50\mu m$, respectively.

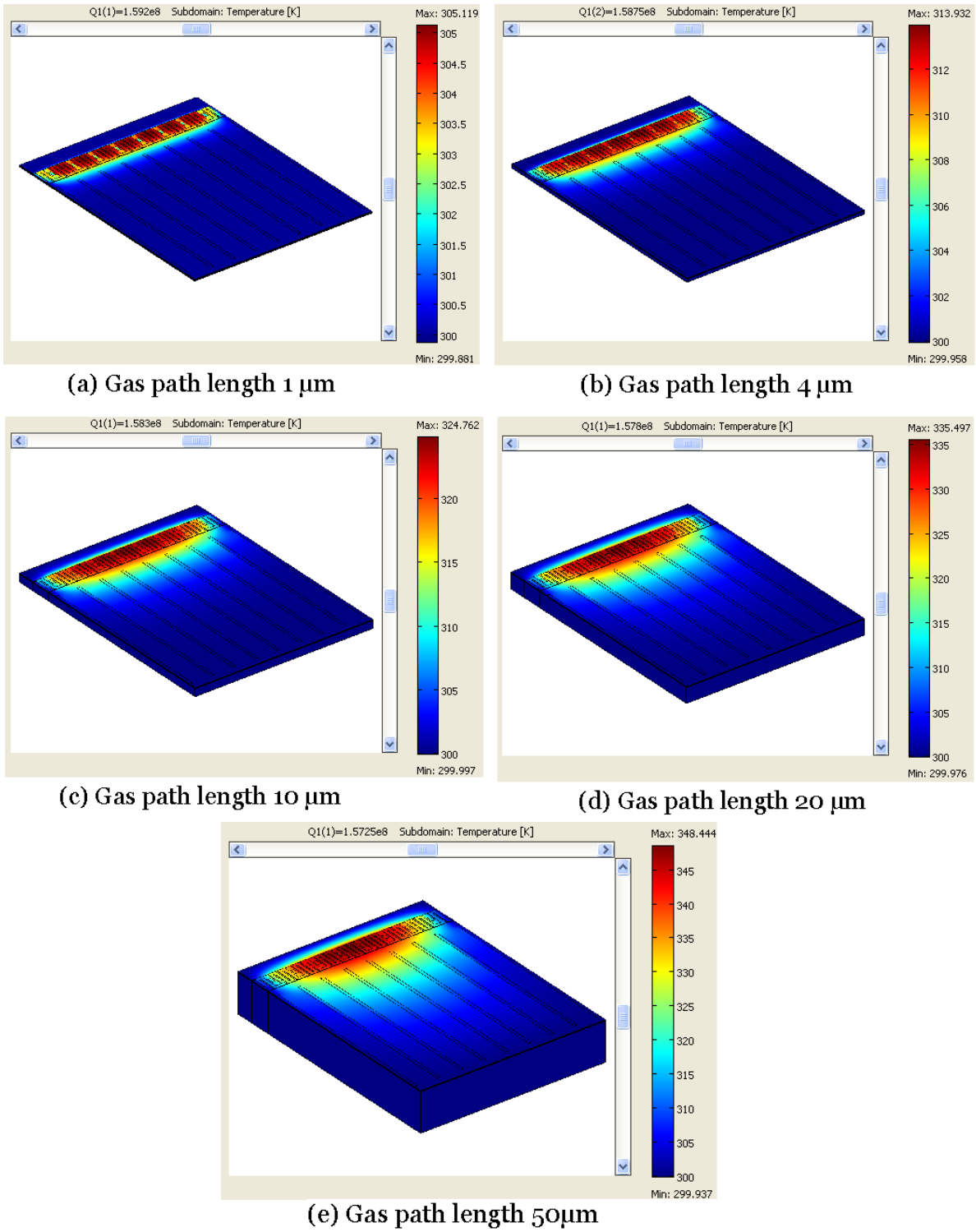

Figure 4.18: Simulated gas sensors with gas path length of $1\mu m$, $4\mu m$, $10\mu m$, $20\mu m$, $50\mu m$

The relationship between the sensitivity and the beam length is shown in Figure 4.19. It is obvious that the sensor sensitivity increases with the gas path length in the simulated range.

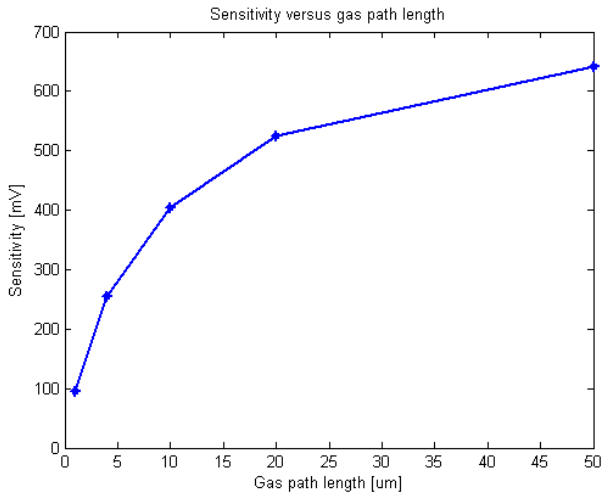

Figure 4.19: Sensitivity versus gas path length

Consider the limitation of the fabrication process, the gas path length should be less than 20 μm. Consequently, the sensor with beam length 260μm and gas path length 20μm is the optimal structure, while its **sensitivity increases by 3.96 times** (from 132.5944573 mV to 524.967744 mV).

4.1.4.5 Larger Gas Opening on the Edge

An improved sensor with larger gas openings placed on the edges of beam is shown in Figure 4.20.

This method is due to the fact that on the two ends of the resistor, the temperature distribution is significantly influenced by the cold edges, and will not change as rapidly with changes in the measured gas as the temperature in the middle part of the heater. Consequently, **the thermocouples should not be placed near the cold edges on the beam.**

Instead, larger gas openings placed on the edges of beam. Besides, **this measure allow the detected gas to flow in the chamber underneath the sensor more**

easily and increase the thermal isolation of the membrane which leads to higher sensor sensitivity. Consequently, **the sensitivity of the improved gas sensor increases by 5.17 times** (from 132.5944573 mV to **684.7970583 mV**).

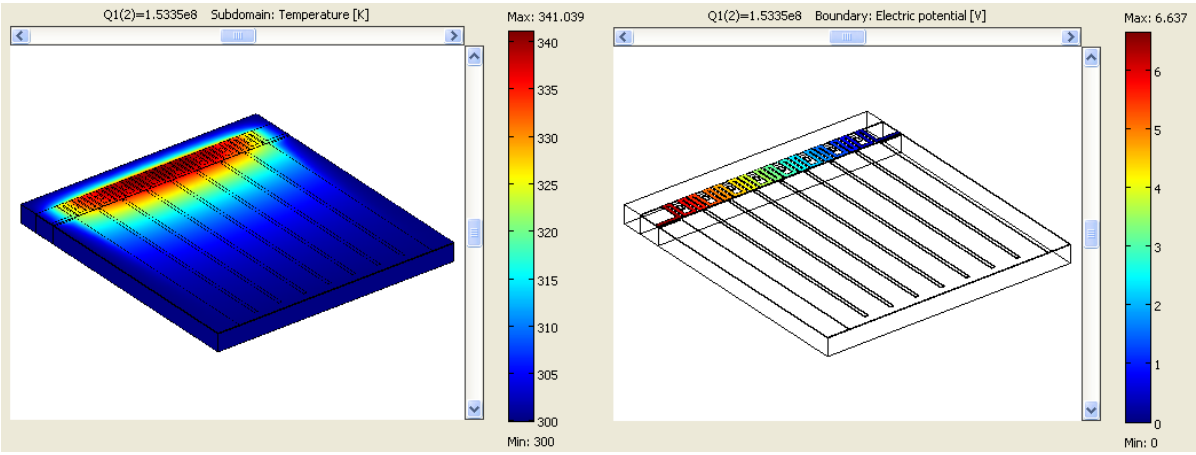

(a) temperature and electric potential distribution

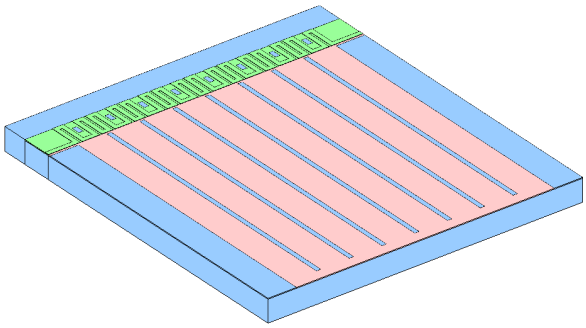

(b) different layers

Figure 4.20: Improved sensor with larger gas openings

4.1.5 Comparison with Analytical Simulation

Gas Path Length

This section will find out the agreement of the numerical simulation and analytical simulation on the relationship between the sensor sensitivity and the gas path length. The simulated gas sensors in Figure 4.21 are all with beam length of $100\mu m$ and with gas path length of $1\mu m$, $5\mu m$, $10\mu m$, $15\mu m$, $20\mu m$, $50\mu m$, respectively.

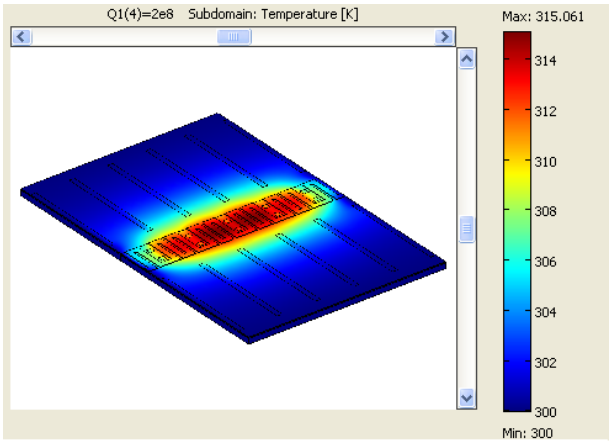

(a) gas path length of $1\mu m$

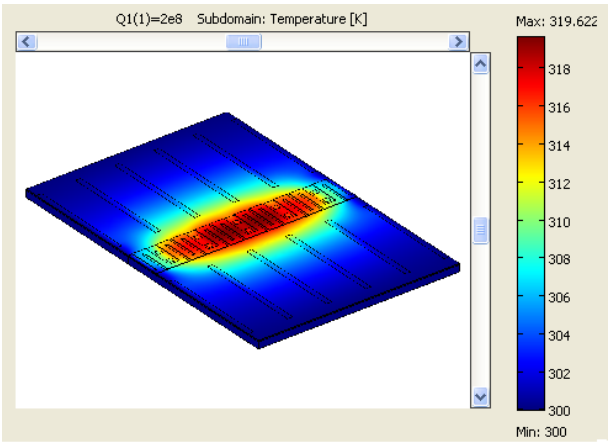

(b) gas path length of $5\mu m$

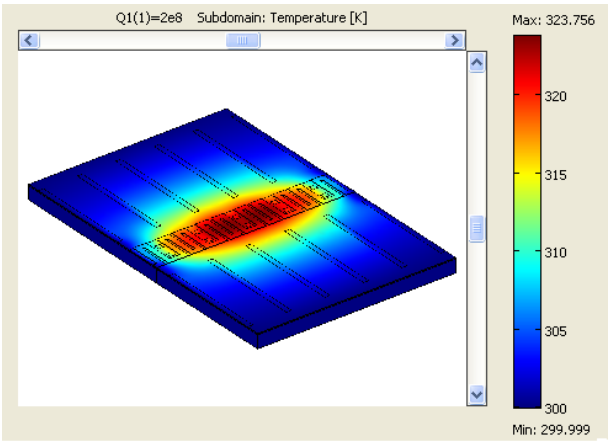

(c) gas path length of $10\mu m$

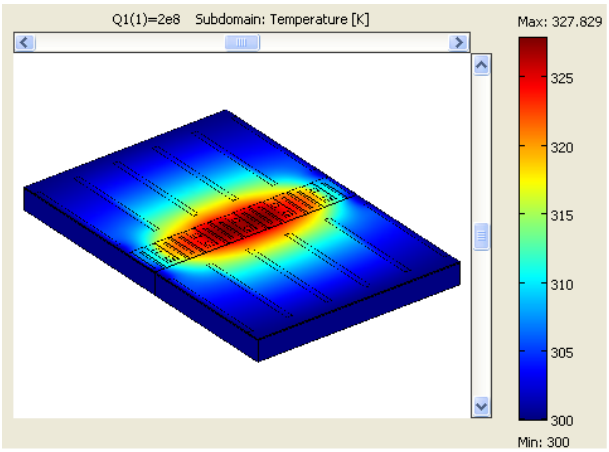

(d) gas path length of $15\mu m$

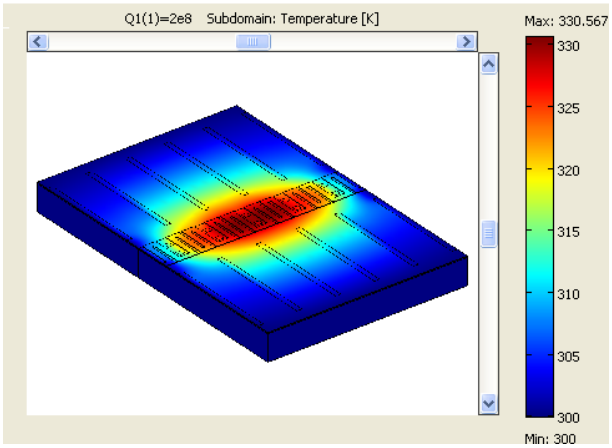

(e) gas path length of $20\mu m$

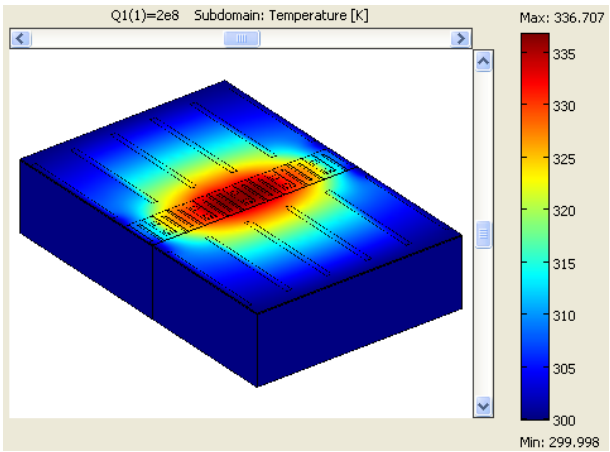

(f) gas path length of $50\mu m$

Figure 4.21: Simulated gas sensors with different gas path lengths

The resulting relationship by COMSOL simulation between the sensor sensitivity and the gas path length is shown in Figure 4.22. There is a **optimal value of gas path length** around $15\mu m$.

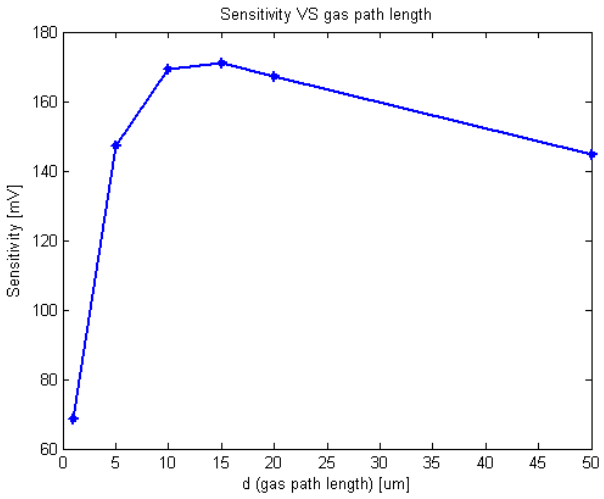

Figure 4.22: Sensitivity versus gas path length - **numerical simulation** COMSOL

The analytical simulation results of the relationship of the sensor sensitivity and the gas path length is shown in Figure 4.23. There is a **optimal value of gas path length** also around $15\mu m$. **The numerical simulation results by COMSOL show the same trend with the analytical simulation results by Matlab.**

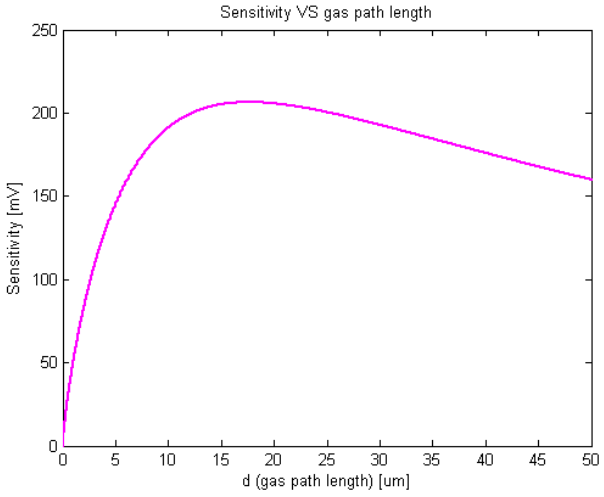

Figure 4.23: Sensitivity versus gas path length - **analytical simulation**

4.2 Conclusions

- An improved sensor based on a **single-clamped bridge** structure with **large gas openings** increase the sensitivity of the sensor by **5.17 times** (from 132.5944573 mV to **684.7970583 mV**). **Large gas openings increase the thermal isolation of the membrane and allow the detected gas to flow in the chamber underneath the sensor more easily.**

- **The thermocouples should not be placed near the cold edges on the beam.** The reason is that **on the two ends of the resistor, the temperature distribution is significantly influenced by the cold edges, and will not change as rapidly with changes in the measured gas as the temperature in the middle part of the heater. Instead, larger gas openings are placed on the edges of beam.**

- **The sensor sensitivity increases with the number of thermocouples.**

- **The numerical simulation results by COMSOL show the same trend with the analytical simulation results by Matlab.**
  The sensor sensitivity increases with the beam length and will be saturated at optimal beam length, and there is a optimal value of gas path length.

Chapter 5

Measurement and Validation

In this chapter, four measurement setups will be presented to show the validation of vacuum pressure measurement and carbon dioxide detection based on this thermal conductivity gas sensor.
Vacuum pressure measurement was implemented to obtain the accurate results of the sensitivity of sensor devices with different features.
For safety consideration, the carbon dioxide is utilized instead of hydrogen in the measurements. Besides, the thermal conductivity difference between carbon dioxide ($0.01465\,{}^{W}/_{m\cdot k}$) and air is only 5.93% of that between hydrogen and air; consequently, an achievement in carbon dioxide detection means an extremely high sensor sensitivity to hydrogen detection.

5.1 Vacuum Pressure Measurement

5.1.1 Measurement Setup

The vacuum pressure measurement setup is shown in Figure 5.1.
A Keithley 236 is used as the current source to feed current into the resistor, while a Keithley 6514 measures the voltage, current and resistance of the resistor. An Agilent 34220A nanovoltmeter measures the output Seebeck voltage from the thermopiles. The device is placed inside the vacuum chamber.

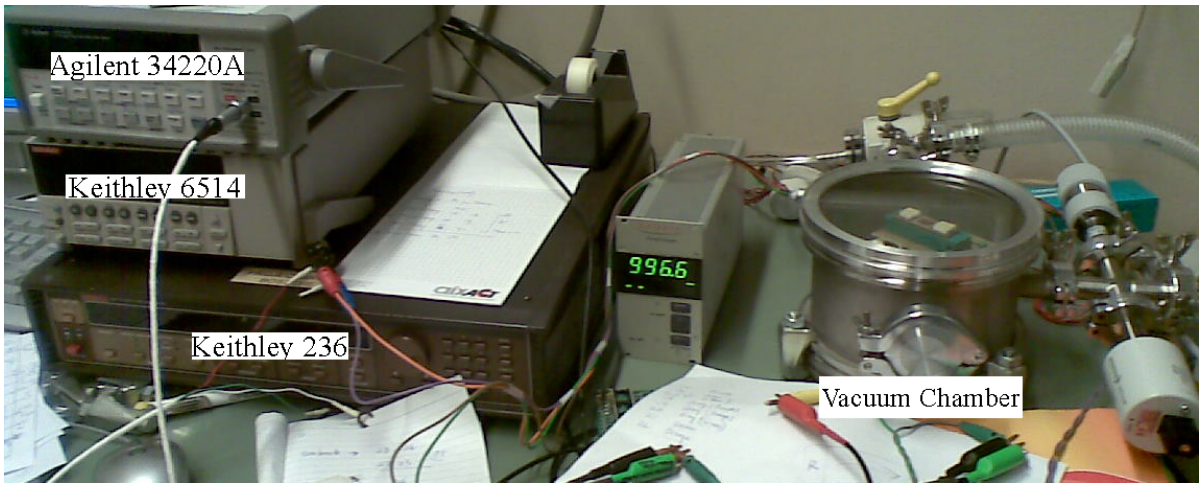

Figure 5.1: Vacuum Pressure Measurement Setup

5.1.2 Measurement Results

In this measurement, four devices are utilized to measure the vacuum pressure. The fabricated devices photos, structure parameters and measurement results are shown as follows.

Device 1: Beam width 154μm, beam length 100μm, total sensor length 232μm.

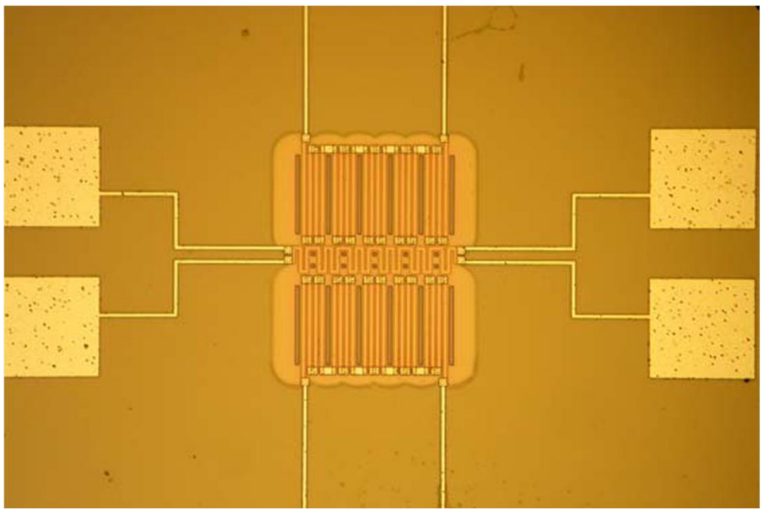

Figure 5.2: Fabricated thermal conductivity sensor: Device 1

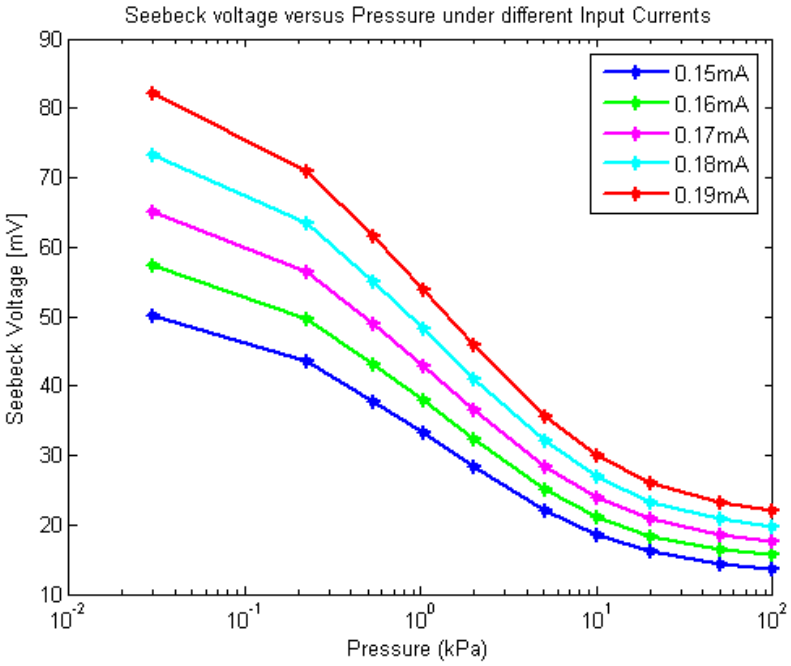

Figure 5.3: Measurement results of device 1: Seebeck voltage versus vacuum pressure

Device 2: Beam width 154μm, beam length 150μm, total sensor length 332μm.

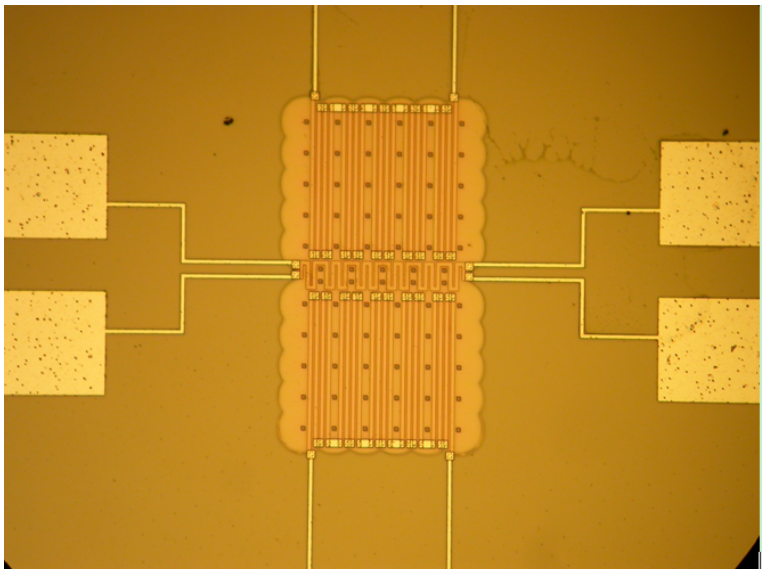

Figure 5.4: Fabricated thermal conductivity sensor: Device 2

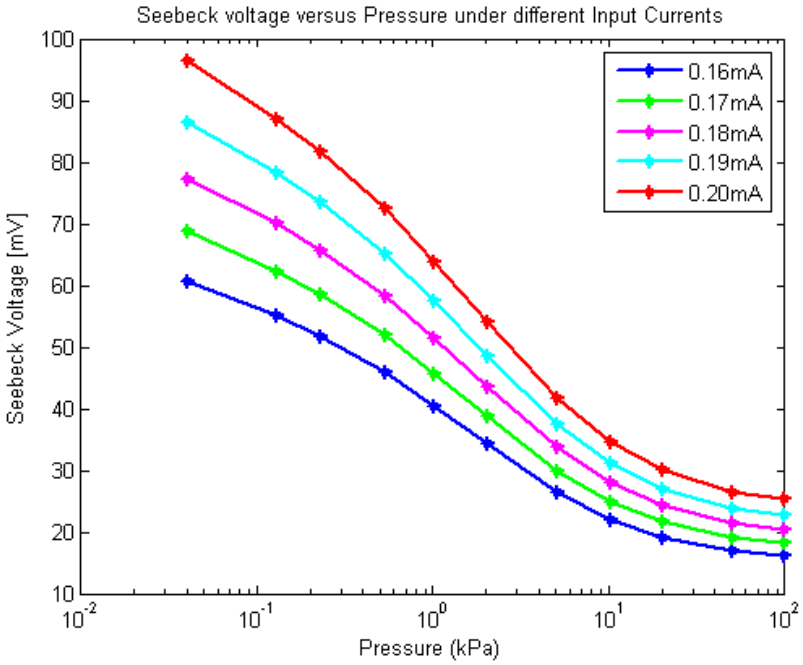

Figure 5.5: Measurement results of device 2: Seebeck voltage versus vacuum pressure

Device 3: Beam width 244µm, beam length 200µm, total sensor length 432µm.

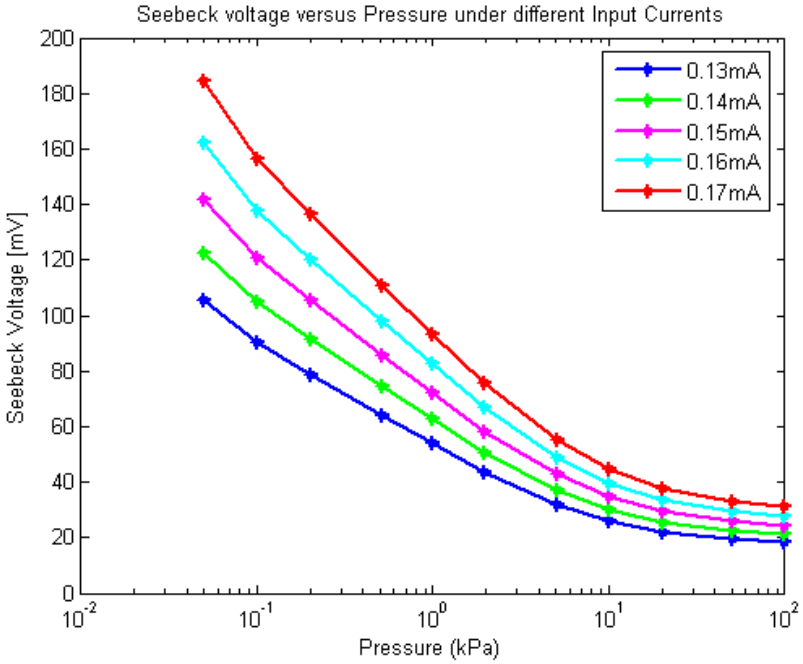

Figure 5.6: Measurement results of device 3: Seebeck voltage versus vacuum pressure

Device 5: Beam width 154μm, beam length 150μm, total sensor length 332μm.

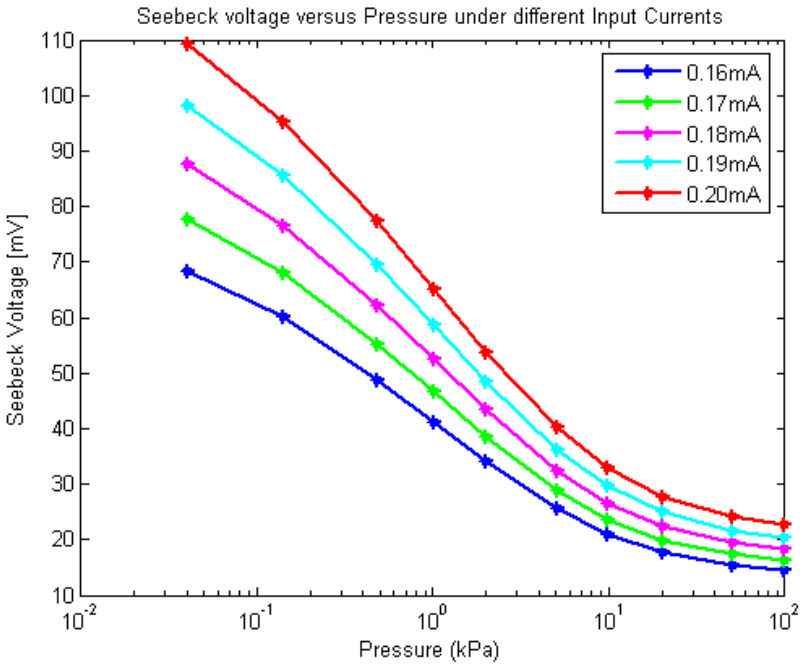

Figure 5.7: Measurement results of device 5: Seebeck voltage versus vacuum pressure

5.1.3 Results Analysis

The measurement results in the Figure 5.3, Figure 5.5 , Figure 5.6 and Figure 5.7 clearly demonstrate that

- the output Seebeck voltage changes with the vacuum pressure; which means the vacuum pressure measurement from 0.3kPa to 100kPa (atmosphere pressure) is accomplished.
- **A higher input current leads to a higher input power, which results in a higher sensor sensitivity**; that shows the same trend in analytical analysis shown in Figure 3.7 in Chapter 3.

Figure 5.8 shows the comparison of the sensitivity of devices with the same input

power of **0.85mW**. The conclusions are drawn as follows.

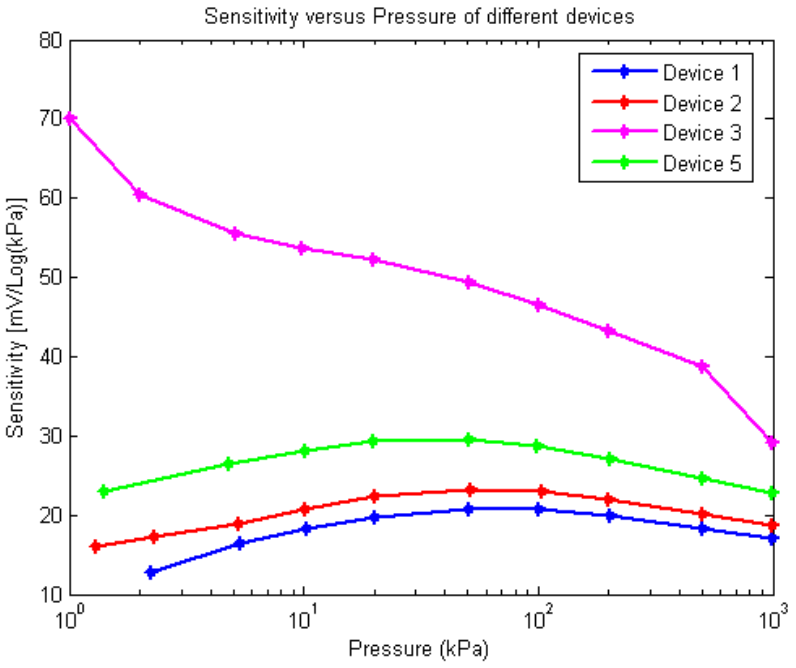

Figure 5.8: Comparison of measurement results of device 1, 2, 3, 5: Seebeck voltage versus vacuum pressure

- Comparison of device 1 and device 5:
  Device 5 has a higher sensitivity than device 1, since device 5 has longer beam length (150μm) than device 1 (100μm) and the same number of thermocouples and gas path length with device 1. This confirms the same trend that **the sensitivity increases with the beam length** as in the analytical analysis shown in Figure 3.9 in Chapter 3 and the numerical analysis shown in Figure 4.14 in Chapter 4.

- Comparison of device 2 and device 5:
  Device 5 has a higher sensitivity than device 2, since device 5 consists larger gas openings than device 2. **Larger gas openings allow the detected gas to flow in the chamber underneath the sensor more easily and increase the thermal isolation of the membrane, consequently, obtain a higher sensitivity.** This measurement results confirm the discussion in the section 4.1.4.5 Larger Gas Opening on the Edge in Chapter 4.

- Comparison of device 3 and device 1:
  Device 3 has a much higher sensitivity than device 1, since device 3 has longer beam length (200μm) beam length than device 1 (100μm) and 6 more pairs of thermocouples than device 1. This not only confirms **the same trend that the sensitivity increases with the beam length as in the analytical analysis** shown in Figure 3.9 in Chapter 3 and the numerical analysis shown in Figure 4.14 in Chapter 4, but also **the same trend that the sensitivity increases with the number of thermocouples as in the numerical analysis** shown in Figure 4.12 in Chapter 4.

5.2 Carbon Dioxide Detection

5.2.1 DC Measurement Setup 1

5.2.1.1 Measurement Setup and Measurement results

As shown in Figure 5.13, Keithley 2400 is used as a source-meter and a current source to feed the input current into the resistor of the sensor, while measure the voltage and current and resistance of the resistor with 4-wire configuration with offset compensation. Agilent 34220A is a voltmeter to measure the output Seebeck Voltage from the thermopile.

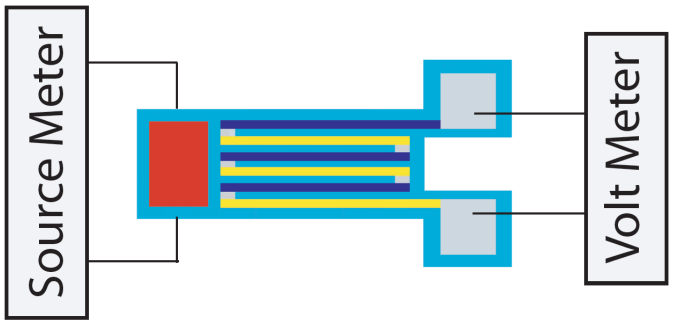

Figure 5.9: Measurement Setup 1

The measurement results in Figure 5.10 indicate that the **output Seebeck voltage changes with the carbon dioxide concentration in air**. An increase in

the carbon dioxide concentration in air leads to an increase in the output Seebeck voltage of 2.26mV at 1.2mW input power. A 100% increase in the carbon dioxide concentration in air leads to an increase in the output Seebeck voltage of 9.98mV at 1.2mW input power.

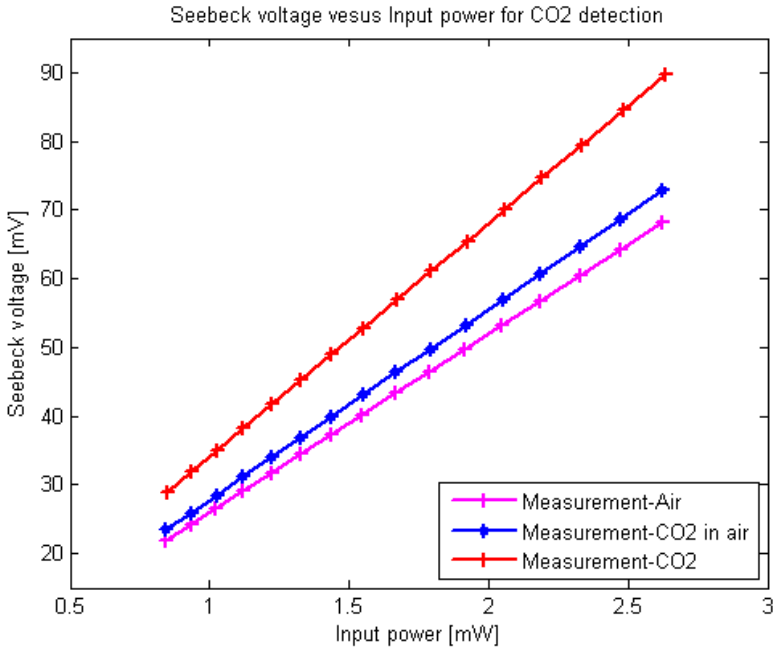

Figure 5.10: Seebeck voltage versus Input power for CO2 detection: setup 1

5.2.1.2 Compare with Numerical Simulation

The measurement and simulation results in Figure 5.11 show that **the increase in output Seebeck voltage with the carbon dioxide concentration in air is in direct ratio to the input power.** The measurement results show that a 100% increase in the carbon dioxide concentration in air leads to an increase in the output Seebeck voltage of 9.98mV at 1.2mW input power. And the simulation results show that a 100% increase in the carbon dioxide concentration in air leads to an increase in the output Seebeck voltage of 9.74mV at 1.2mW input power.

Figure 5.12 shows the deviation between the measurement and simulation results. The simulation results is validated by the measurement results since they result in **an error less than 2.36%.**

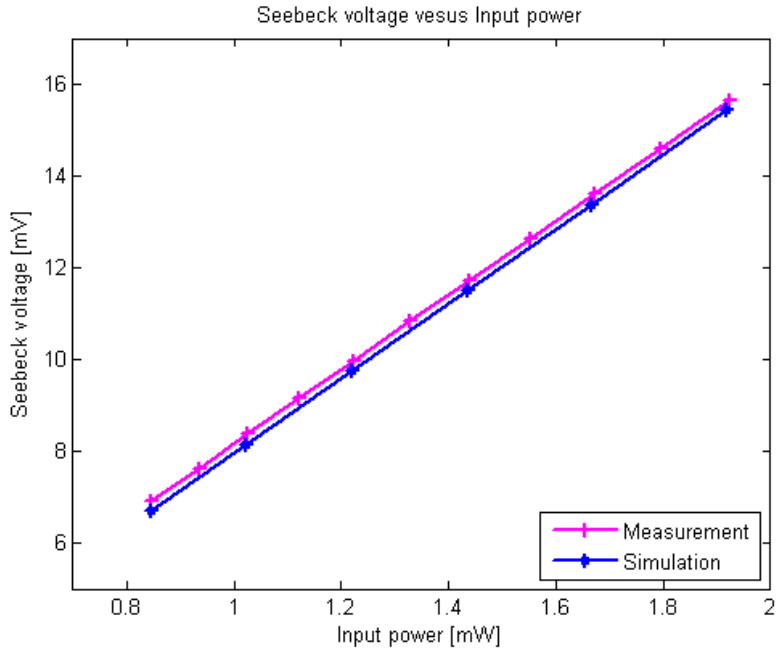

Figure 5.11: Seebeck voltage versus Input power for CO2 detection: setup 1

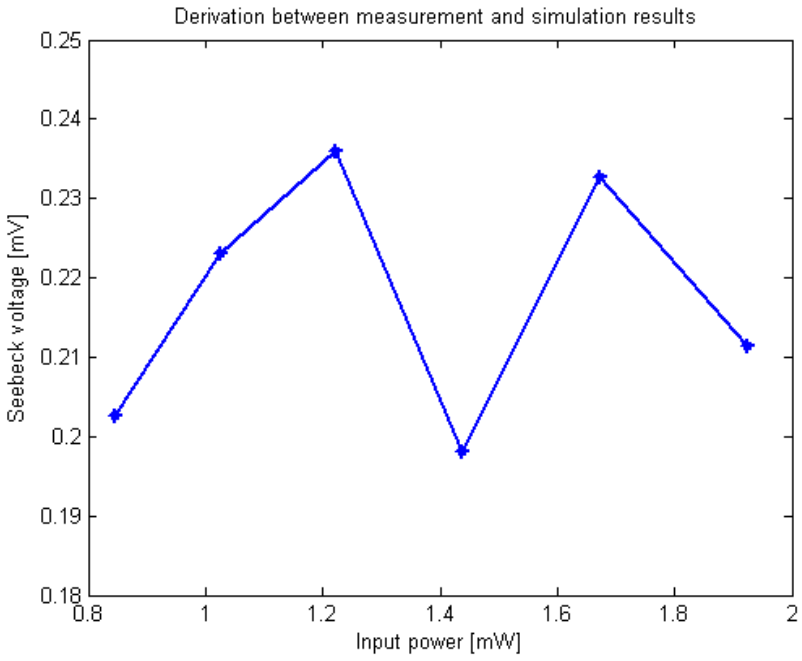

Figure 5.12: Seebeck voltage versus Input power for CO2 detection: setup 1

5.2.1.3 Detection Limit

The detection limit is the minimum concentration of the carbon dioxide in air that can be measured, and is mainly determined by the DC offset and the noise.

DC offset

Since the thermopile is offset-free, and the DC offset from the nanovoltmeter Agilent 34220A is cancelled by its offset compensation, the DC offset V_{os2} is only due to the biasing current and is expressed as

$$V_{os2} = I_{bias} \cdot R_{th}$$

in which I_{bias} is the biasing current of the nanovoltmeter Agilent 34220A which is smaller than 50 pA, R_{th} is the resistance of thermopile which is 54 $k\Omega$.

Because the output of this sensor system is the increase in output Seebeck voltage with the carbon dioxide concentration in air, which is the difference of two output Seebeck voltages; consequently, the **DC offset is cancelled**.

Noise

The noise from the nanovoltmeter Agilent 34220A is 41 nV_{RMS}.

The thermal noise from the thermopile is expressed by

$$V_{n,R} = \sqrt{4k \cdot T \cdot R_{th} \cdot f}$$

in which the k is the Boltzmann constant $1.38 \times 10^{-23} J/K$, T is the temperature, R_{th} is the resistance of thermopile which is 54 $k\Omega$. f is determined by the filter in nanovoltmeter Agilent 34220A.

The selected digital filter MEDIUM mode averages every last 50 readings. The selected measurement function is DCV and the selected display digits is $7\frac{1}{2}$, which means the Reading speed is 0.15 readings/s. Consequently, the filter bandwidth is only 0.003Hz.

The thermal noise is equal to:

$$V_{n,R} = \sqrt{4 \times 1.38 \times 10^{-23} \times 350 \times 54 \times 10^{3} \times 0.003} = 1.769[\text{nV}]$$

Thus the equivalent noise is

$$V_n = \sqrt{(1.769)^2 + \left(41 \times \sqrt{2}\right)^2} = 58.01[\text{nV}]$$

and is **dominated by the noise from the nanovoltmeter Agilent 34220A**.

Detection Limit

The detection limit is the minimum concentration of the carbon dioxide in air that can be measured, and is mainly determined by the noise. Consequently, the relationship of the noise and the carbon dioxide concentration in air need to be obtain. The detected increasement in the output Seebeck voltage is 9.98mV with a 100% increase in the carbon dioxide concentration in air at 1.2mW input power. And the corresponding change in thermal conductivity is $0.00929\,{}^{\text{W}}/_{\text{m·k}}$ with 100% increase in the carbon dioxide concentration in air. Consequently, the corresponding change in thermal conductivity with the 58.01nV noise is $5.40 \times 10^{-8}\,{}^{\text{W}}/_{\text{m·k}}$, which leads to **a detection limit of 0.00058 %** in the carbon dioxide concentration in air at 1.2mW input power.

5.2.2 DC Measurement Setup 2

5.2.2.1 Measurement Setup and Measurement results (with AD620)

As shown in Figure 5.13, a Keithley 2400 is used as a source-meter and a current source to feed the input current into the resistor of the sensor, while measure the voltage and current and resistance of the resistor with 4-wire configuration with offset compensation. A low-cost low-offset low-noise instrumentation amplifier AD620 is utilized to amplify the extremely small Seebeck voltage and filter the interference noise. An Agilent 34220A is used as a voltmeter to measure the output Seebeck Voltage from the thermopile.

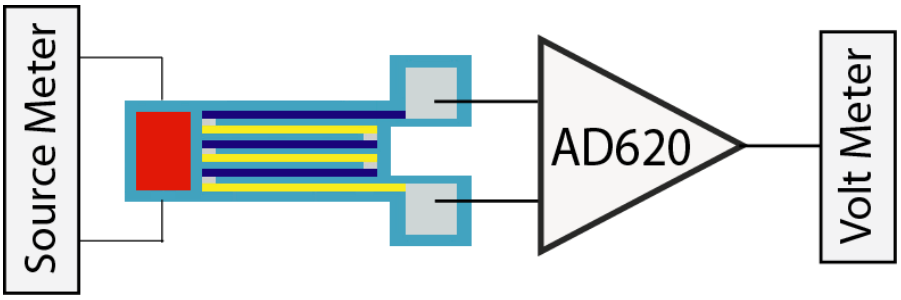

Figure 5.13: Measurement Setup 2

The measurement results in Figure 5.14 indicate that the **amplified output Seebeck voltage changes with the carbon dioxide concentration in air**. An increase in the carbon dioxide concentration in air leads to an increase in the amplified output Seebeck voltage of 166.43mV at 0.6mW input power. And **this increase in amplified output Seebeck voltage is in direct ratio to the input power.**

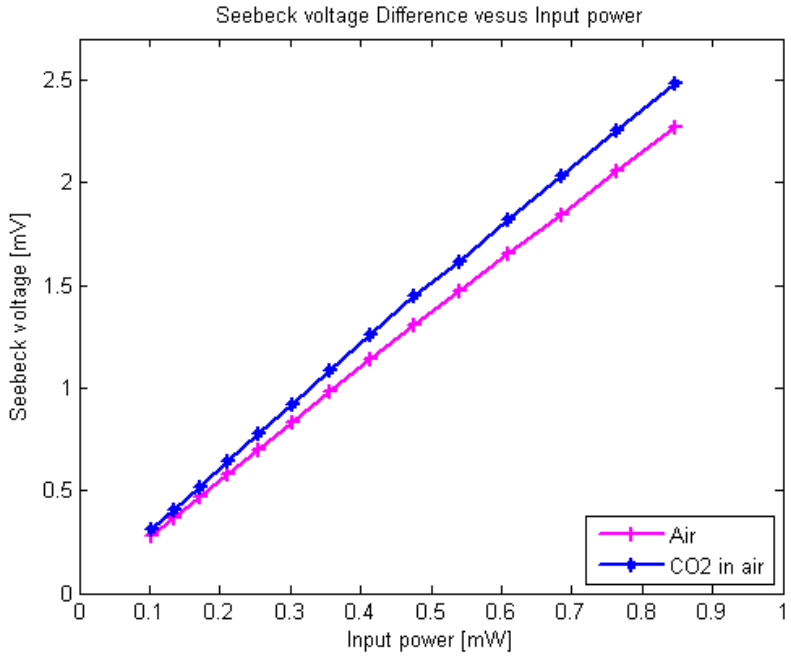

Figure 5.14: Seebeck voltage versus Input power for CO2 detection: setup 2

5.2.2.2 Detection Limit

The detection limit is determined by the DC offset and the noise.

DC offset

Since the thermopile is offset-free, and the gain of the AD 620 is 106 which is rather large, consequently, the DC offset from the the nanovoltmeter Agilent 34220A can be neglected. Thus the DC offset is composed of two parts: the DC offset V_{os1} from the AD 620 which is $30\mu V$, and the DC offset V_{os2} due to the biasing current

$$V_{os2} = I_{bias} \cdot R_{th}$$

in which I_{bias} is the biasing current of the nanovoltmeter Agilent 34220A which is smaller than 50 pA, R_{th} is the resistance of thermopile which is 54 $k\Omega$.

Because the output of this sensor system is the increase in output Seebeck voltage with the carbon dioxide concentration in air, which is the difference of two output Seebeck voltages; consequently, the **DC offset is cancelled**.

Noise

The noise from the AD620 is 22 nV/$\sqrt{\text{Hz}}$.

The thermal noise from the thermopile is expressed by

$$V_{n,R} = \sqrt{4k \cdot T \cdot R_{th} \cdot f}$$

in which the k is the Boltzmann constant $1.38 \times 10^{-23} J/K$, T is the temperature, R_{th} is the resistance of thermopile which is 54 $k\Omega$. f is determined by the filter in nanovoltmeter Agilent 34220A which is 0.003Hz as calculated in last section.

The thermal noise is equal to:

$$V_{n,R} = \sqrt{4 \times 1.38 \times 10^{-23} \times 350 \times 54 \times 10^3 \times 0.003} = 1.769[\text{nV}]$$

Thus the equivalent noise is

$$V_n = \sqrt{(1.769)^2 + \left(22 \times \sqrt{0.003}\right)^2} = 2.14[\text{nV}]$$

and is **dominated by the thermal noise from the sensor.**

Detection Limit

The detection limit is the minimum concentration of the carbon dioxide in air that can be measured, and is mainly determined by the noise. Consequently, the relationship of the noise and the corresponding carbon dioxide concentration in air need to be obtained. The detected increasement in the output Seebeck voltage is 166.43 mV with a 100% increase in the carbon dioxide concentration in air at 0.6 mW input power. And the corresponding change in thermal conductivity is 0.00929 $^{W}/_{m\cdot k}$ with 100% increase in the carbon dioxide concentration in air. Consequently, the corresponding change in thermal conductivity with the 2.14nV noise is 1.99×10^{-9} $^{W}/_{m\cdot k}$, which leads to **a detection limit of 0.0000214 %** in the carbon dioxide concentration in air at 0.6mW input power.

5.3 AC Measurement Setup

The AC measurement setup shown in Figure 5.15 is based on lock-in amplification.

Lock-in amplification is a technique used to separate the small, narrow-band signal from interfering noise. Very small Seebeck voltage signals can be detected in the presence of large amounts of uncorrelated noise with known frequency and phase.

A 20Hz AC sine wave is applied on the resistor of sensor, which results in a 40Hz AC sine wave with 90^o phase shift electrical power on the resistor. the resistor coverts the input electrical power into heat power which leads to hot temperature. Consequently, the output Seebeck voltage from thermopile is a 40Hz AC sine wave with 90^o phase shift . The lock-in-amplifier SR830 is used to detect the 40Hz AC sine wave Seebeck voltage.

As shown in Figure 5.16, the detected increasement in the output Seebeck voltage is 5mV with 100 kPa air to 0.05kPa vacuum with $1.5V_{RMS}$ AC input voltage. This shows that the gas detection is accomplished.

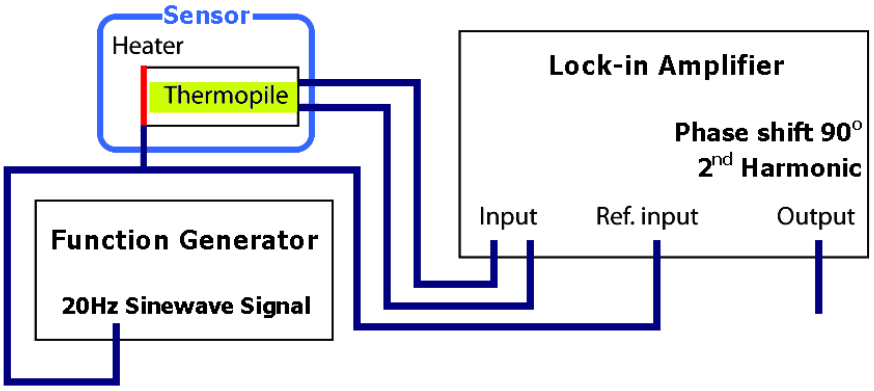

Figure 5.15: AC measurement Setup

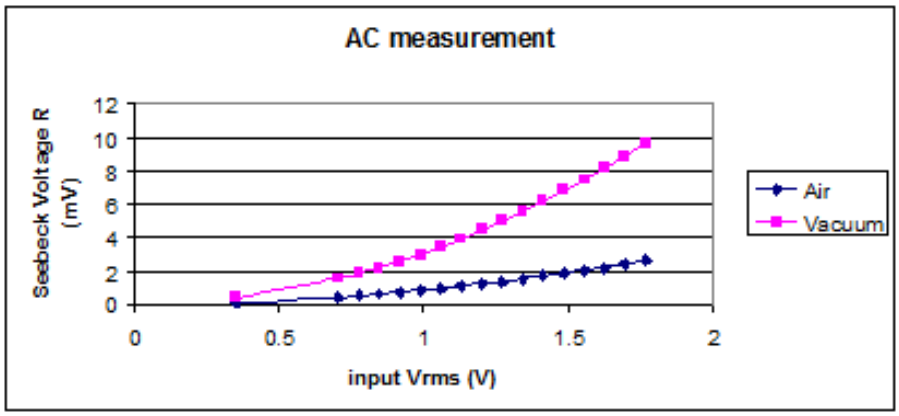

Figure 5.16: Seebeck voltage versus Input power for vacuum detection

AC Noise

The noise from SR830 is 6 nV/$\sqrt{\text{Hz}}$.

The thermal noise from the thermopile is expressed by

$$V_{n,R} = \sqrt{4k \cdot T \cdot R_{th} \cdot f}$$

in which the k is the Boltzmann constant $1.38 \times 10^{-23} J/K$, T is the temperature, R_{th} is the resistance of thermopile which is 54 $k\Omega$. f is determined by the input signal which is 20 Hz.

The thermal noise is equal to:

$$V_{n,R} = \sqrt{4 \times 1.38 \times 10^{-23} \times 350 \times 54 \times 10^3 \cdot 20} = 144.44[\text{nV}]$$

Thus the equivalent noise is

$$V_n = \sqrt{(144.44)^2 + \left(6 \times \sqrt{20}\right)^2} = 146.91[\text{nV}]$$

and is **dominated by the thermal noise from the sensor.**

The detected increasement in the output Seebeck voltage is 5mV with 100 kPa air to 0.05kPa vacuum with $1.5V_{RMS}$ AC input voltage. And the noise is only 0.00294% of the detected increasement.

5.4 Conclusions

Vacuum pressure measurement was implemented to obtain the accurate results of the sensitivity of sensor devices with different features.

Vacuum pressure measurement

- The output Seebeck voltage changes with the vacuum pressure; the vacuum pressure measurement from 0.3kPa to 100kPa is accomplished.
- A higher input current leads to a higher input power, which results in a higher sensor sensitivity; that shows the same trend in analytical analysis shown in Chapter 3.
- **Larger gas openings allows the detected gas to flow in the chamber underneath the sensor more easily and increase the thermal isolation of the membrane, consequently, obtain a higher sensitivity.** This confirm the discussion and numerical simulations in COMSOL in the section 4.1.4.5 Larger Gas Opening on the Edge in Chapter 4.

- **The sensitivity increases with the beam length** and **the number of thermocouples.** This confirm the discussion in the analytical analysis and the numerical analysis.

For safety consideration, the carbon dioxide is utilized instead of hydrogen in measurements. Besides, the thermal conductivity difference between carbon dioxide ($0.01465\,{}^{W}/_{m\cdot k}$) and air is only 5.93% of that between hydrogen and air; consequently, an achievement in carbon dioxide detection means an extremely high sensor sensitivity to hydrogen detection.

Carbon Dioxide Detection

- The measurement results confirm that the **output Seebeck voltage changes with the carbon dioxide concentration in air**. And **the increase in output Seebeck voltage is in direct ratio to the input power.** A 100% increase in the carbon dioxide concentration in air leads to an increase in the output Seebeck voltage of 9.98mV at 1.2mW input power. The simulation results and the measurement results result in **an error less than 2.36%.**

- The output signal is the difference between two output Seebeck voltages; consequently, the **DC offset is cancelled**.

- The low-cost low-offset low-noise instrumentation amplifier AD620 is utilized to amplify the extremely small Seebeck voltage and suppress the interference noise from the next stage: nanovoltmeter. **A detection limit of 0.0000214 %** in the carbon dioxide concentration in air at 0.6mW input power is obtained with instrumentation amplifier instead of **0.00058 %** when without instrumentation amplifier.

AC measurement setup

- Lock-in amplifier is used to separate the small, narrow-band Seebeck voltage signal from interfering noise.

- The AC noise is only 0.00294% of the detected increasement in Seebeck voltage with $1.5V_{RMS}$ AC input voltage.

Chapter 6

Conclusions

This chapter concluded the thermal conductivity gas sensor on its application, principle, fabrication, analytical analysis, numerical analysis, measurements and sensor performance.

Application:

Thermal conductivity sensors are especially suitable for hydrogen detection, since the thermal conductivity of hydrogen is approximately 7.5 times that of the air. It indicates that even very low concentration of hydrogen leakage in air is still possible to be detected. Therefore, thermal conductivity gas sensors are especially suitable for detection of the leakage of hydrogen before hydrogen concentrations reach the lower explosive limit (LEL) of 4% in air in safety applications.

Principle:

The thermal conductivity gas sensor performs a measurement of the thermal conductivity of measurand gas. By feeding current into the resistor in the center of the sensor, the resistor is heated up and becomes a "hot element". Then, the measurand gas transfers a quantity of heat from the hot resistor to the cold edge via the thermal conduction through the measured gas, which leads to a decrease in the temperature of resistor. Thus, for a given experimental configuration and a fixed input power, **the changes in the thermal conductivity of measurand gas can be detected by measuring the changes in the temperature of resistor**.

Fabrication:

In order to **improve the sensor sensitivity by minimizing the heat loss to the suspended membrane** without any complex fabrication steps, **a simple floating membrane structured** micro-thermoelectric gas sensor is fabricated **using surface micromachining**.

Analytical analysis:

- Consider the limitation of the fabrication process, a optimal sensor sensitivity of **568.8** mV is obtained for 1.2mW input power hydrogen detection with beam length 280μm and gas path length 20 μm in thermal modeling using Matlab.
- The thermal modeling shows that **there is a optimum value of the gas path length for each beam length.**
  When the gas path length is rather short, the temperature of heater is greatly influenced by the underneath cold substrate, which result in a low sensitivity to the changes in the thermal conductivity of measurand gas.
  When the gas path length is rather long, less heat from the heater will conducted through the gas, and more heat will lost through the beam, thus the temperature of heater has a lower sensitivity to the changes in the thermal conductivity of measurand gas.
- The radiation effects can be neglected at temperature below 636.8K.

Numerical analysis:

- An improved sensor based on a **single-clamped bridge** structure with **large gas openings** increase the sensitivity of the sensor by **5.17 times**. **Large gas openings increase the thermal isolation of the membrane and allow the detected gas to flow in the chamber underneath the sensor more easily.**
- **The thermocouples should not be placed near the cold edges on the beam.** The reason is that **on the two ends of the resistor, the temperature distribution is significantly influenced by the cold edges, and**

will not change as rapidly with changes in the measured gas as the temperature in the middle part of the heater. Instead, larger gas openings are placed on the edges of beam.

- **The sensor sensitivity increases with the number of thermocouples.**

- **The numerical simulation results by COMSOL show the same trend with the analytical simulation results by Matlab.**
  The sensor sensitivity increases with the beam length and will be saturated at optimal beam length, and there is a optimal value of gas path length.

Measurements:

Vacuum pressure measurement

- The output Seebeck voltage changes with the vacuum pressure; the vacuum pressure measurement from 0.3kPa to 100kPa is accomplished.

- A higher input current leads to a higher input power, which results in a higher sensor sensitivity; that shows the same trend in analytical analysis.

- **Larger gas openings allows the detected gas to flow in the chamber underneath the sensor more easily and increase the thermal isolation of the membrane, consequently, obtain a higher sensitivity.** This confirm the the discussion and simulations in the numerical analysis.

- **The sensitivity increases with the beam length** and **the number of thermocouples.** This confirm the discussion and simulations in the analytical analysis and the numerical analysis.

Carbon Dioxide Detection

- For safety consideration, the carbon dioxide is utilized instead of hydrogen in measurements. Besides, an achievement in carbon dioxide detection means an extremely high sensor sensitivity to hydrogen detection.

- The measurement results confirm that the **output Seebeck voltage changes with the carbon dioxide concentration in air**. And **the increase in output Seebeck voltage is in direct ratio to the input power.** A 100% increase in the carbon dioxide concentration in air leads to an increase in the output Seebeck voltage of 9.98mV at 1.2mW input power. The simulation results and the measurement results result in **an error less than 2.36%.**

- The output signal is the difference between two output Seebeck voltages; consequently, the **DC offset is cancelled**.

- The low-cost low-offset low-noise instrumentation amplifier AD620 is utilized to amplify the extremely small Seebeck voltage and suppress the interference noise from the next stage. **A detection limit of 0.0000214 %** in the carbon dioxide concentration in air at 0.6mW input power is obtained with instrumentation amplifier instead of **0.00058 %** when without instrumentation amplifier.

AC measurement setup

- Lock-in amplifier is used to separate the small, narrow-band Seebeck voltage signal from interfering noise.

- The AC noise is only 0.00294% of the detected increasement in Seebeck voltage with $1.5V_{RMS}$ AC input voltage.

Sensor Performance:

Sensitivity, response time, power consumption, stability, detection limit are the main performances that need to be considered in gas sensors. **Thermal conductivity sensors have enhanced long-term stability and a faster response time compared with chemical sensors.**

The sensor in this work has a much **higher sensitivity, a lower input power and a better detection limit** than other compared sensors as shown in Table 6.1.

Table 6.1: Comparison of Sensors Performance

	Sensitivity [mV]	**Input Power** [mW]	**Sensitivity /Power** [V/W]	**Response Time** [s]	**Detection limit**	**Stability**
[28]	160 (Hydrogen in air)	Catalytic activation energy	–	7 s	0.1% - 2% Hydrogen	poor
[29]	48 (Hydrogen in air)	10.42	4.61 (Hydrogen in air)	36 ms	0.1% - 2% Hydrogen	good
[31]	250 (Ethane in methane)	59.50	4.20 (Ethane in methane)	–	–	good
this work	**684.8** (Hydrogen in air)	**1.2**	**570.7** (Hydrogen in air)	–	**0.0000214 %** (Carbon dioxide in air)	good

Bibliography

[1] Gas sensors and gas metering: Applications and markets. Technical report, BCC Research, 2005.

[2] L. Brett. Hydrogen safety sensors and their applications in hydrogen storage, distribution and use. Technical report, European Commission's Joint Research Center, 2003.

[3] J.L. Cruz D. Zalvidea, A. Diez and M.V. Andres. Hydrogen sensor based on a palladium-coated fibre-taper with improved time-response. *Sensors and Actuators*, 114:268–274, 2006.

[4] Olaf Schulz Jan Spannhake, Andreas Helwig and Gerhard Müller. *Solid State Gas Sensing*, chapter Micro-Fabrication of Gas Sensors, pages 1–46. Springer US, 2009.

[5] Isolde Simon and Michael Arndt. Thermal and gas-sensing properties of a micromachined thermal conductivity sensor for the detection of hydrogen in automotive applications. *Sensors and Actuators A: Physical*, 97-98:104–108, 2002.

[6] Claude Lucat Pascal Tardy, Jean-René Coulon and Francis Menil. Dynamic thermal conductivity sensor for gas detection. *Sensors and Actuators B: Chemical*, 98:63–68, 2004.

[7] M. Baraton. Optimizing chemical gas sensors using ir spectroscopy. *SPIE Newsroom*, 2009.

[8] Otto S. Wolfbeis. Fiber-optic chemical sensors and biosensors. *Analytical Chemistry*, 80:4269–4283, 2008.

[9] Radhika Dasari and Francis P. Zamborini. Hydrogen switches and sensors fabricated by combining electropolymerization and pd electrodeposition at microgap electrodes. *Journal of the American Chemical Society*, 130:16138–16139, 2008.

[10] M. P.; Xiao Z. L.; Rosenmann D.; Welp U.; Kwok W. K.; Xu, T.; Zach and G. W. Crabtree. Self-assembled monolayer-enhanced hydrogen sensing with ultrathin palladium films. *Applied Physics Letters*, 86:203104 – 203104–3, 2005.

[11] Richard P. Vasquez Mangesh A. Bangar Nosang V. Myung Eric J. Menke Reginald M. Penner Yeonho Im, Choonsup Lee and Minhee Yun. Investigation of a single pd nanowire for use as a hydrogen sensor. *Small*, 2:356–358, 2006.

[12] L B Luo H Wang C S Lee Z H Chen, J S Jie and S T Lee. Applications of silicon nanowires functionalized with palladium nanoparticles in hydrogen sensors. *Nanotechnology*, 18, 2007.

[13] H. Xia Z. Zhao, M.A. Carpenter and D. Welch. All-optical hydrogen sensor based on a high alloy content palladium thin film. *Sensors and Actuators*, 113:532–538, 2006.

[14] Fu-Chun Huang; Yung-Yu Chen; and Tsung-Tsong Wu. A room temperature surface acoustic wave hydrogen sensor with pt coated zno nanorods. *Nanotechnology*, 20, 2009.

[15] Inc. Wolfram Research. http://www.periodictable.com/.

[16] AIR LIQUIDE. http://encyclopedia.airliquide.com/Encyclopedia.asp.

[17] CPO Science. 27.1 conduction. www.cpo.com/ipcres/pdfs/unit9/Ch27Sec1.pdf.

[18] Wikipedia. http://en.wikipedia.org/wiki/Heat transfer.

[19] Wikipedia. http://en.wikipedia.org/wiki/Second law of thermodynamics.

[20] Wikipedia. http://en.wikipedia.org/wiki/Thermal conductivity.

[21] Wikipedia. http://en.wikipedia.org/wiki/Thermoelectric effect.

[22] M. Sauer A. Graf, M. Arndt and G. Gerlach. Review of micromachined thermopiles for infrared detection. *Measurement Science and Technology*, 18:59–75, 2007.

[23] A.W. van Herwaarden. *Thermal Sensors (in Smart Sensor Systems)*. John Wiley &Sons, 2008.

[24] Wikipedia. http://en.wikipedia.org/wiki/Thermistor.

[25] L. Francioso R. Rella P. Siciliano J. Spadavecchia D. S. Presicce A. M. Taurino S. Capone, A. Forleo. Solid state gas sensors: state of the art and future activities. *Journal of Optoelectronics and Advanced Materials*, 5:1335–1348, 2003.

[26] G. Eranna; B. C. Joshi; D. P. Runthala and R. P. Gupta. Oxide materials for development of integrated gas sensors - a comprehensive review. *Critical Reviews in Solid State and Material Sciences*, 29:111–118, 2004.

[27] Luyuan Zhang Dong Xiang Chengxiang Wang, Longwei Yin and Rui Gao. Metal oxide gas sensors: Sensitivity and influencing factors. *Sensors journal*, 10:2088–2106, 2010.

[28] Chung-il Lee Yong-Jun Kim Se-Chul Park, Seung-Il Yoon and Soonho Song. A micro-thermoelectric gas sensor for detection of hydrogen and atomic oxygen. *Analyst*, 134:236–242, 2009.

[29] Xensor Integration. Tcg-3880 data sheet, 2008. http://www.xensor.nl/.

[30] A.W. van Herwaarden. Overview of calorimeter chips for various applications. *Thermochimica Acta*, 432:192–201, 2005.

[31] G. Carles J. Santander L. Fonseca S. Udina, M. Carmona and S. Marco. A micromachined thermoelectric sensor for natural gas analysis: Thermal model and experimental results. *Sensors and Actuators B: Chemical*, 134:551–558, 2008.

[32] ROGER T. HOWE JAMES M. BUSTILLO and RICHARD S. MULLER. Surface micromachining for microelectromechanical systems. *Proceedings of the IEEE*, 86:1552–1574, 1998.

[33] Y. C. Tai C. H. Mastrangelo and R. S. Muller. *Journal of Applied Physics*, 63:1442–1447, 1988.

[34] A. Jain X.J. Hu and K.E. Goodson. Investigation of the natural convection boundary condition in microfabricated structures. *International Journal of Thermal Sciences*, 47:820–824, 2008.

[35] Wikipedia. http://en.wikipedia.org/wiki/Heat equation.

[36] N.; van Herwaarden A.W.; Schellevis H.; Wien W.H.A.; Nanver L.K. La Spina, L.; Nenadovic. Mems test structure for measuring thermal conductivity of thin films. *IEEE International Conference on Microelectronic Test Structures, 2006. ICMTS 2006.*, pages 137–142, 2006.

Appendices

Appendix A

Equivalent Thermal Conductivity Model

Due to the symmetry of whole sensor structure, only one pair of thermocouple and the corresponding part of beam (as shown in Fig A.1) are modelled in analytical calculation of equivalent thermal conductivity model.

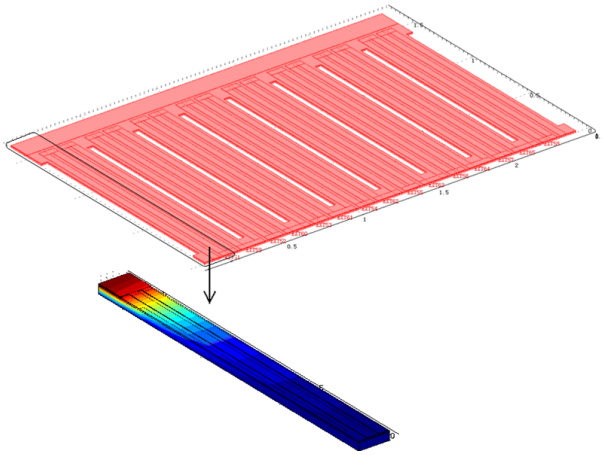

Figure A.1: simplified model for 1D analytical calculation

Description of Layers

a. 1st low stress SiN 700nm

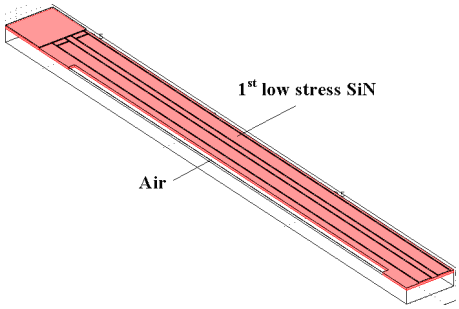

Figure A.2:

Thermal conductivity $\lambda_{SiN1} = 1.3\,{}^{\mathrm{W}}/_{\mathrm{m\cdot k}}$

Beam length $L_{SiN1} = 116\mu m$

beam thickness $t_{SiN1} = 700nm$

beam width $W_{SiN1} = 12\mu m$

b. Low stress PolySi 300nm

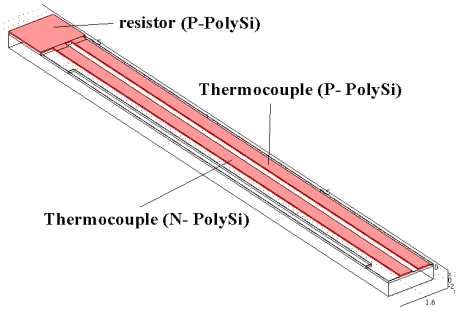

Figure A.3:

Resistor (P-Poly-Si)[36]:

$$\lambda_{Resistor} = 34\,{}^{\mathrm{W}}/_{\mathrm{m\cdot k}},\ L_{Resistor} = 14\,\mu m,$$

$$t_{Resistor} = 300\,nm,\ W_{Resistor} = 15\,\mu m$$

Thermocouple (P- Poly Si) [36]:

$$\lambda_{p-PolySi} = 34\,{}^{\mathrm{W}}/_{\mathrm{m\cdot k}},\ L_{p-PolySi} = 102\,\mu m,$$

$$t_{p-PolySi} = 300\,nm,\ W_{p-PolySi} = 4\,\mu m$$

Thermocouple (N- Poly Si) [36]:

$$\lambda_{n-PolySi} = 29\,{}^{\mathrm{W}}/_{\mathrm{m\cdot k}},\ L_{n-PolySi} = 102\,\mu m,$$

$$t_{n-PolySi} = 300\,nm,\ W_{n-PolySi} = 4\,\mu m$$

c. 2nd low stress SiN 100nm

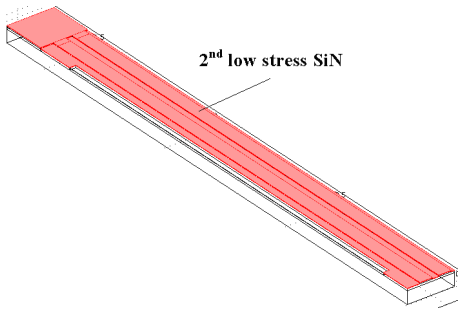

Figure A.4:

$$\lambda_{SiN2} = 1.3\,{}^{\mathrm{W}}/_{\mathrm{m\cdot k}},\ L_{SiN2} = 116\,\mu m,$$

$$t_{SiN2} = 100\,nm,\ W_{SiN2} = 13\,\mu m$$

d. Al contact 600nm (ignored in the model)

$$\lambda_{Al} = 237\,{}^{\mathrm{W}}/_{\mathrm{m\cdot k}},\ L_{Al} = 8\,\mu m,$$

$$t_{Al} = 600\,nm,\ W_{Al} = 10\,\mu m\ or\ 13\,\mu m$$

Equivalent thermal conductivity calculation

a. SiN Layers

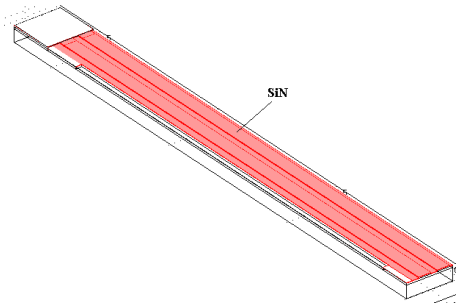

Figure A.5: SiN layers for analytical calculation

The analytical calculation of 1st and 2nd SiN layers only involves the colored part in Fig A.5. The two small SiN boxes are neglected because their thermal conductances are quite small compared to the rest SiN part.
Thus the thermal conductance is calculated as follow:

$$\lambda_{SiN} = 1.3\,{}^{\mathrm{W}}/_{\mathrm{m\cdot k}},\ L_{SiN} = 102\,\mu m,$$

$$t_{SiN} = 800\,nm,\ W_{SiN} = 12\,\mu m$$

equivalent thermal conductance

$$\begin{aligned} g_{SiN} &= \lambda_{SiN} \cdot \frac{W_{SiN} \cdot t_{SiN}}{L_{SiN}} \\ &= 1.3 \times \frac{(12 \times 10^{-6}) \times (800 \times 10^{-9})}{102 \times 10^{-6}} \\ &= 12.235 \times 10^{-8} [{}^{\mathrm{W}}/_{\mathrm{K}}] \end{aligned}$$

b. Thermocouple (P- PolySi and N- PolySi)

Thermocouple (P- PolySi):

$\lambda_{P-PolySi}$= 34 ${}^{\mathrm{W}}/_{\mathrm{m\cdot k}}$ [36], $L_{P-PolySi}$ = 102 μm,

$t_{P-PolySi}$ = 300 nm, $W_{P-PolySi}$ = 4 μm

equivalent thermal conductance

$$\begin{aligned} g_{P-PolySi} &= \lambda_{P-PolySi} \cdot \frac{W_{P-PolySi} \cdot t_{P-PolySi}}{L_{P-PolySi}} \\ &= 34 \times \frac{(4 \times 10^{-6}) \times (300 \times 10^{-9})}{102 \times 10^{-6}} \\ &= 40 \times 10^{-8} [{}^{\mathrm{W}}/_{\mathrm{K}}] \end{aligned}$$

Thermocouple (N- PolySi):

$\lambda_{N-PolySi}$= 29 ${}^{\mathrm{W}}/_{\mathrm{m\cdot k}}$ [36], $L_{N-PolySi}$ = 102 μm,

$t_{N-PolySi}$ = 300 nm, $W_{N-PolySi}$ = 4 μm

equivalent thermal conductance

$$\begin{aligned} g_{N-PolySi} &= \lambda_{N-PolySi} \cdot \frac{W_{N-PolySi} \cdot t_{N-PolySi}}{L_{N-PolySi}} \\ &= 29 \times \frac{(4 \times 10^{-6}) \times (300 \times 10^{-9})}{102 \times 10^{-6}} \\ &= 34.12 \times 10^{-8} [\mathrm{W/K}] \end{aligned}$$

c. Al contact

Al contact is neglected because the thermal conductivity of Al (237 $\mathrm{W/m \cdot k}$) is significantly large compared with that of SiN (1.3 $\mathrm{W/m \cdot k}$). And when the thermal resistances are in series, the thermal conductance should be added as

$$g_{Al\&SiN} = \frac{1}{\frac{1}{g_{Al}} + \frac{1}{g_{SiN}}}$$

Since $\frac{1}{g_{Al}}$ is considerably larger than $\frac{1}{g_{SiN}}$, Al contact can be ignored.

d. Entire beam

equivalent thermal conductance is express as

$$\begin{aligned} g_{eq} &= \lambda_{eq} \cdot \frac{W_{eq} \cdot t_{eq}}{L_{eq}} \\ &= g_{SiN} + g_{P-PolySi} + g_{N-PolySi} \\ &= \lambda_{eq} \frac{W_{SiN} \cdot t_{SiN} + W_{P-PolySi} \cdot t_{P-PolySi} + W_{N-PolySi} \cdot t_{N-PolySi}}{L_{eq}} \end{aligned}$$

in which

$$\begin{aligned} g_{SiN} + g_{P-PolySi} + g_{N-PolySi} &= 12.235 \times 10^{-8} + 40 \times 10^{-8} + 34.12 \times 10^{-8} \\ &= 86.355 \times 10^{-8} [\mathrm{W/K}] \end{aligned}$$

$$\begin{aligned} & \lambda_{eq} \cdot \frac{W_{SiN} \cdot t_{SiN} + W_{P-PolySi} \cdot t_{P-PolySi} + W_{N-PolySi} \cdot t_{N-PolySi}}{L_{eq}} \\ = \quad & \lambda_{eq} \frac{(12 \times 10^{-6}) \times (800 \times 10^{-9}) + (4 \times 10^{-6}) \times (300 \times 10^{-9}) \times 2}{102 \times 10^{-6}} \end{aligned}$$

.

Thus, equivalent thermal conductivity is λ_{eq}= 7.34 $\mathrm{W/m \cdot k}$,

equivalent beam length is L_{eq} = 102 μm,

equivalent beam thickness is t_{eq} = 884.6 nm,

equivalent beam width is W_{eq} = 12 μm

Appendix B

A Part of MATLAB Codes

```
clear all
clc
close all

s = 0.19;
b = 5.67*10^(-8);

k = 0.03;
cmeagas = 0.1805;

cair = 0.02394;
cgas = k*cmeagas + (1 - k)*cair;

ts = 0.9*10^(-6);
cs = 6.3;

Ta = 300;

Lres = 28*10^(-6);

W = 154*10^(-6);
Pin = 0.6;
nt = 10;
a = 290/1000000;


Lbeam=100;
d=[0:0.001:50];

C1 = sqrt((4* s .* b * Ta^3 + cair./d/10^(-6))/(ts*cs));
```

```
C2 = sqrt((4* s .* b * Ta^3 + cgas./d/10^(-6))/(ts*cs));

Ti1 = Pin./(C1*W*ts*cs.*(C1*Lres ...
    + coth(C1*(Lbeam*10^(-6)- Lres))));

Ti2 = Pin./(C2*W*ts*cs.*(C2*Lres ...
    + coth(C2*(Lbeam*10^(-6)- Lres))));

Sensitivity = abs(a*nt*(Ti1 - Ti2))/k;

figure(1)
plot(d,Sensitivity,'m','Linewidth',1.5);
%axis([0 20 0 40])
xlabel('d (gas path length) [um]');
ylabel('Sensitivity [mV]');
title('Sensitivity VS gas path length')



Lbeam_2=[28:10:500];
d_2=20;

C1_2 = sqrt((4* s .* b * Ta^3 + cair./d_2/10^(-6))...
    /(ts*cs));
C2_2 = sqrt((4* s .* b * Ta^3 + cgas./d_2/10^(-6))...
    /(ts*cs));


Ti1_2 = Pin./(C1_2*W*ts*cs.*(C1_2*Lres+ coth(C1_2.*...
    (Lbeam_2.*10^(-6) - Lres))))+300;

Ti2_2 = Pin./(C2_2*W*ts*cs.*(C2_2*Lres+ coth(C2_2.*...
    (Lbeam_2.*10^(-6) - Lres))))+300;

Sensitivity_2 = abs(a*nt*(Ti1_2 - Ti2_2))/k

figure(3)
plot(Lbeam_2,Sensitivity_2);
%axis([0 20 0 50])
xlabel('Lbeam (beam length) [um]');
ylabel('Sensitivity [mV]');
title('Sensitivity VS beam length when d=20um')

d_3=[0.001:1.5:50];
Lbeam_3=[50:20:500];

for va=1:length(d_3)
    for vb=1:length(Lbeam_3)
        C1_3 = sqrt((4* s .* b * Ta^3 ...
```

```
            + cair/d_3(va)/10^(-6))/(ts*cs));
        C2_3 = sqrt((4* s .* b * Ta^3 ...
            + cgas/d_3(va)/10^(-6))/(ts*cs));


        Ti1_3 = Pin./(C1_3*W*ts*cs*(C1_3*Lres...
            + coth(C1_3*(Lbeam_3(vb)*10^(-6) - Lres))))+300;

        Ti2_3 = Pin./(C2_3*W*ts*cs*(C2_3*Lres...
            + coth(C2_3*(Lbeam_3(vb)*10^(-6) - Lres))))+300;


        Sensitivity_3(va,vb) = abs(a*nt*(Ti1_3 - Ti2_3))/k;
    end
end

figure(4)
surf(Lbeam_3,d_3,Sensitivity_3);
%axis([0 500 0 50 0 1000])
title('Sensitivity VS beam length and gas path length')
xlabel('Lbeam (beam length) [um]')
ylabel('d (gas path length) [um]')
zlabel('Sensitivity [mV]')


d_4=[0.001:0.01:250];
Lbeam_4=[50:50:300];

for va=1:length(d_4)
    for vb=1:length(Lbeam_4)
        C1_4 = sqrt((4* s .* b * Ta^3 ...
            + cair/d_4(va)/10^(-6))/(ts*cs));
        C2_4 = sqrt((4* s .* b * Ta^3 ...
            + cgas/d_4(va)/10^(-6))/(ts*cs));


        Ti1_4 = Pin./(C1_4*W*ts*cs*(C1_4*Lres...
             + coth(C1_4*(Lbeam_4(vb)*10^(-6) - Lres))))+300;

        Ti2_4 = Pin./(C2_4*W*ts*cs*(C2_4*Lres...
             + coth(C2_4*(Lbeam_4(vb)*10^(-6) - Lres))))+300;


        Sensitivity_4(va,vb) = abs(a*nt*(Ti1_4 - Ti2_4))/k;
    end
end

figure(5)
plot(d_4,Sensitivity_4,'LineWidth',1.5);
```

```
legend('Lbeam=50um','Lbeam=100um','Lbeam=150um',...
      'Lbeam=200um','Lbeam=250um','Lbeam=300um',4);
%axis([0 100 0 100])
title('Sensitivity VS gas path length at different beam lengths')
ylabel('Sensitivity [mV]')
xlabel('d (gas path length) [um]')
zlabel('Sensitivity [mV]')



d_6=[1 5 10 20 50];
Lbeam_6=[30:0.1:500];

for vb=1:length(Lbeam_6)
    for va=1:length(d_6)
        C1_6 = sqrt((4* s .* b * Ta^3 ...
            + cair/d_6(va)/10^(-6))/(ts*cs));
        C2_6 = sqrt((4* s .* b * Ta^3 ...
            + cgas/d_6(va)/10^(-6))/(ts*cs));


        Ti1_6 = Pin./(C1_6*W*ts*cs*(C1_6*Lres...
            + coth(C1_6*(Lbeam_6(vb)*10^(-6) - Lres))))+300;

        Ti2_6 = Pin./(C2_6*W*ts*cs*(C2_6*Lres ...
            + coth(C2_6*(Lbeam_6(vb)*10^(-6) - Lres))))+300;


        Sensitivity_6(vb,va) = abs(a*nt*(Ti1_6 - Ti2_6))/k;
    end
end

figure(6)
plot(Lbeam_6,Sensitivity_6,'LineWidth',1.5);
legend('d=1um','d=5um','d=10um','d=20um','d=50um',4);
%axis([0 100 0 100])
title('Sensitivity VS gas path length at different beam lengths')
ylabel('Sensitivity [mV]')
xlabel('d (gas path length) [um]')
zlabel('Sensitivity [mV]')
```

```
clear
clc
s = 0.19;
b = 5.67*10^(-8);

k = 0.03;
```

```
cmeagas = 0.1805;

cair = 0.02394;
cgas = k*cmeagas + (1 - k)*cair;

ts = 0.9*10^(-6);
cs = 6.3;

Ta = 300;

Lres = 28*10^(-6);

Lbeam = 100*10^(-6);
W = 154*10^(-6);

nt = 10;
a = 290/1000000;

d = 4*10^(-6);

Pin = 0:0.000001:2;

C1 = sqrt((4* s * b * Ta^3 + cair/d)/(ts*cs));
C2 = sqrt((4* s * b * Ta^3 + cgas/d)/(ts*cs));


Ti1 = Pin/(C1*W*ts*cs*(C1*Lres + coth(C1*(Lbeam - Lres))));

Ti2 = Pin/(C2*W*ts*cs*(C2*Lres + coth(C2*(Lbeam - Lres))));
Sensitivity = abs(a*nt*(Ti1 - Ti2))/k;

plot(Pin,Sensitivity,'Linewidth',1.5)
title('Sensitivity VS Input Power ')
xlabel('Input Power [mW]')
ylabel('Sensitivity [mV]')
```

```
clc
clear all
close all

x1= [1,4,10,20,50]

y1= [95.37260933
254.561043
405.0588533
524.967744
642.426879]
```

```
12
13 figure(1)
14 plot (x1, y1, '-b*','LineWidth',2);%grid on;
15
16
17 xlabel('Gas path length [um]');
18 ylabel('Sensitivity [mV]');
19 title('Sensitivity versus gas path length')
```

```
1  clc
2  clear all
3  close all
4
5  x1= [50,100,150,210,260,300]
6
7  y1= [275.912148
8  450.4361297
9  501.752925
10 522.916922
11 524.967744
12 525.769594]
13
14
15
16 figure(1)
17 plot (x1, y1, '-b*','LineWidth',2);%grid on;
18
19
20 xlabel('Beam length [um]');
21 ylabel('Sensitivity [mV]');
22 title('Sensitivity versus beam length')
```

```
1  clc
2  clear all
3  close all
4
5  x1= [8,10,12,16]
6
7  y1= [183.0588267
8  209.852265
9  231.560302
10 253.6427967]
11
12
13 figure(1)
```

```
plot (x1, y1, '-b*','LineWidth',2);%grid on;
axis([6 18 160 280])

xlabel('Number of thermocouples');
ylabel('Sensitivity [mV]');
title('Sensitivity versus number of thermocouples')
```

```
clc
clear all
close all

x3= [0.84531674

1.024071133

1.220322265

1.434287069

1.666342144

1.916518276]


y3=[21.949916

26.598573

31.705012

37.275514

43.321202

49.843446]


x5= [0.846513669

1.025830623

1.222830114

1.437765873

1.671078226

```

```
41 1.922846882]
42
43
44 y5= [28.866888
45
46 34.975327
47
48 41.683164
49
50 48.997855
51
52 56.933911
53 65.492217]
54
55
56
57 y0= y5-y3
58
59 x8=[0.8444
60 1.02344
61 1.22016
62 1.43442
63 1.66684
64 1.9173]
65
66 y8=[6.71431113
67 8.15372642
68 9.74217213
69 11.52426331
70 13.38007307
71 15.4373902]
72
73 z=y0-y8
74
75
76 figure(1)
77 % plot (x5, y0, '-m+', x8,y8,'-b*','LineWidth',2);%grid on;
78 plot (x5, z, '-b*', 'LineWidth',2);%grid on;
79  axis ([0.8 2 0.18 0.25])
80
81 % plot (x4,y5,'-b*','LineWidth',2);%grid on;
82 % legend('Measurement-Air','Measurement-CO2 in air','Measurement-CO2',4);
83 %legend('Measurement','Simulation',4);
84
85 xlabel('Input power [mW]');
86 ylabel('Seebeck voltage [mV]');
87 %title('The change of Seebeck voltage vesus Input power for CO2 detection')
88 title('Derivation between measurement and simulation results ')
```

```
clc
clear all
close all


x3= [0.103133541
0.134721356
0.170551252
0.210600314
0.254853964
0.303392074
0.356196775
0.413305764
0.474686717
0.540383642
0.610352272
0.684673568
0.763302382
0.846276758]


y3=[0.283252
0.370338
0.469157
0.579717
0.701832
0.835818
0.981579
1.139299
1.308915
1.47045
1.651596
1.846845
2.052865
2.267203]


x4= [0.103140355
0.134731705
0.170568219
0.21062676
0.254885647
0.303436828
0.356257629
0.413387498
0.474804904
0.540537954
```

```
 0.610555422
 0.68493449
 0.763630923
 0.846682763]


y4= [0.31281204
 0.40902291
 0.51850298
 0.64066902
 0.77553206
 0.92356346
 1.0846185
 1.2588842
 1.4451597 %
 1.61581
 1.8180288
 2.0330332
 2.2572739
 2.4838877]


x5= [0.846513669
 0.933972435
 1.025830623
 1.122113501
 1.222830114
 1.328037263
 1.437765873
 1.552073083
 1.671078226
 1.794674436
 1.922846882]


y5= [28.866888
 31.847079
 34.975327
 38.253821
 41.683164
 45.264507
 48.997855
 52.886518
 56.933911
 61.135939
 65.492217]


```

```
x8=[0.8444
1.02344
1.22016
1.43442
1.66684
1.9173]

y8=[6.71431113
8.15372642
9.74217213
11.52426331
13.38007307
15.4373902]




figure(1)
% plot (x5, y0, '-m+', x8,y8,'-b*','LineWidth',2);%grid on;
plot (x3, y3, '-m+', x4, y4,'-b*','LineWidth',2);%grid on;
 axis ([0 1 0 2.7])

% plot (x4,y5,'-b*','LineWidth',2);%grid on;
legend('Air','CO2 in air',4);
%legend('Measurement','Simulation',4);

xlabel('Input power [mW]');
ylabel('Seebeck voltage [mV]');

title('Seebeck voltage Difference vesus Input power')
```

```
clc
clear all
close all


x3= [
0.47355
0.8444
1.21992
1.9173
3.4532
5.4875]


y3=[
```

```
16 4.1734411
17 7.4449911
18 10.7580372
19 16.9176686
20 30.5003441
21 48.5382004]
22
23 y4= [
24 3.6272513
25 6.4679924
26 9.3423931
27 14.6801529
28 26.4214366
29 41.9522868]
30
31
32 figure(1)
33
34 plot (x3, y3, '-m+', x3,y4,'-b*','LineWidth',2);%grid on;
35
36 legend('Air','3% H2 in air',4);
37
38 xlabel('Input power [mW]');
39 ylabel('Seebeck voltage [mV]');
40
41 title('Seebeck voltage Difference vesus Input power')
```

Acknowledgments